Journal of South American Earth Sciences 88 (2018) 497–519

Contents lists available at ScienceDirect

Journal of South American Earth Sciences

journal homepage: www.elsevier.com/locate/jsames

Ushuaia pluton: Magma diversification, emplacement and relation with regional tectonics in the southernmost Andes

Mauricio González Guillot[a,b,*], Matías Ghiglione[c,d], Mónica Escayola[b,d], Márcio Martins Pimentel[e,2], James Mortensen[f,1], Rogelio Acevedo[a]

[a] Centro Austral de Investigaciones Científicas (CADIC), CONICET, B. Houssay 200, (V9410BFD), Ushuaia, Argentina
[b] Instituto de Ciencias Polares, Ambiente y Recursos Naturales, Universidad Nacional Tierra Del Fuego, Fuegia Basket 251 (V9410BFD), Ushuaia, Argentina
[c] Instituto de Estudios Andinos IDEAN (Universidad de Buenos Aires), Buenos Aires, Argentina
[d] Consejo Nacional de Investigaciones Científicas y Técnicas (CONICET), Argentina
[e] Instituto de Geociências, Universidade de Brasilia (UnB), 70910-900, Brasilia, Brazil
[f] Pacific Centre for Isotopic and Geochemical Research, Earth & Ocean Sciences, University of British Columbia, 6339 Stores Road, (V6T 1Z4), Vancouver, BC, Canada

ARTICLE INFO

Keywords:
Pluton growth
Magma diversification
Regional tectonics
Late Cretaceous
Fuegian Andes

ABSTRACT

The Ushuaia pluton (UP) and the Ushuaia Peninsula Andesites (UPA) are intrusive units of a Late Cretaceous rear-arc in the Southernmost Andes. We report new LA-ICP-MS zircon ages from ~71 to 75 Ma for the UP, and of ~84 Ma for the UPA, which allow to differentiate these two magmatic events; consistent with their distinct petrography and geochemistry. The UP is a composite, incrementally assembled pluton in upper crustal levels. Successive injections of magma batches define two main sections, each in turn constructed by several smaller pulses: an early ultramafic-mafic section consists mainly of hornblende pyroxenite, hornblendite and gabbro/diorite with reverse concentric zonation, and a later intermediate section built up mainly by monzodiorite. Mingling and layering between mafic and intermediate facies along the contact point to simultaneous emplacement at the end of one main pulse and the beginning of the other. Mineralogy and geochemistry suggest the rock sequence in the UP is cogenetic. In part it resulted by in-situ magmatic processes that included crystal-melt fractionation during injection of magma mushes, mingling, local melt segregation and mixing with crustal partial melts. The country rock is affected by penetrative ductile deformation and regional metamorphism developed during mid-Cretaceous Andean main orogenic phase. It also shows an overimposed pluton-margin parallel foliation and a post-kinematic contact metamorphic aureole. On the other hand, the UP has a concentric igneous foliation parallel to pluton margins interpreted as a primary magmatic feature. The above evidences, along with absence of subsolidus fabrics and metamorphism, indicate the pluton post-date peak regional metamorphism and ductile structures in the country rock. The new zircon ages constrain the top age of early Andean deformation, as well as the magmatic gap registered for the end of the Cretaceous, and confirm an emplacement during a recorded compressive regime that transmitted shortening to the foreland.

1. Introduction

Recent work on pluton growth have shown to be a piecemeal process by in-situ amalgamation of small volumes of magma (Glazner et al., 2004; Annen, 2011; Miller et al., 2011), elapsing a short (~0.1–0.5 m.y.; Michel et al., 2008; Leuthold et al., 2014; Bucholz et al., 2017) or a significant time span (~3–10 m.y.; Coleman et al., 2004; Matzel et al., 2006), with direct relation on the pluton size (de Saint Blanquat et al., 2011). The newly injected magma batches intrude already, or partially, consolidated pulses, depending on injection and cooling rates. Following this ideas, the concepts of magma chamber and in-situ magmatic differentiation have been questioned (Glazner et al., 2004; Barbey, 2009; Annen, 2011; Blundy and Annen, 2016). Moreover, the relation of pluton fabric to regional deformation, as was traditionally seen (e.g. Paterson et al., 1989), was also challenged, since only large plutons are able to register the interaction of regional deformation and the growing body, due to their longer interval of construction, losing the incremental structures. Contrarily, small plutons

* Corresponding author. Centro Austral de Investigaciones Científicas (CADIC), CONICET, B. Houssay 200, (V9410BFD), Ushuaia, Argentina..
E-mail addresses: g_guillot@cadic-conicet.gob.ar, mgonzalez@untdf.edu.ar (M. González Guillot).
[1] Present address: EOS UBC, 2020–2207 Main Mall, Vancouver, BC, Canada V6T 1Z4.
[2] Deceased in July 2018.

https://doi.org/10.1016/j.jsames.2018.10.001
Received 6 April 2018; Received in revised form 29 September 2018; Accepted 2 October 2018
Available online 03 October 2018
0895-9811/

tend to record the incremental process (de Saint Blanquat et al., 2011).

The Ushuaia pluton (UP) is a small (outcrop area of ~8 km^2), isolated intrusion where processes of incremental growth and in-situ magma diversification can be evaluated. It belongs to a suite of monzonitic - mildly alkaline composition formed in a period of potassic magmatism (Fuegian Potassic Magmatism; González Guillot et al., 2009) that was emplaced to the rear of a Late Cretaceous arc in Tierra del Fuego, spatially (although not genetically) related to minor intrusions collectively named *Ushuaia Peninsula Andesites* (González Guillot et al., 2011).

These rear-arc units have not received enough attention and divergent interpretations abound. The UP in particular has been correlated to the Ushuaia Peninsula Andesites (e.g. Peroni et al., 2009); although petrography, geochemistry and age preclude any genetic linkage (González Guillot et al., 2011; this work). Additionally, the tectonic regime during pluton emplacement has not been well constrained so far. While some authors point out a transtensional scenario (Peroni et al., 2009), our U–Pb zircon crystallization ages indicate that emplacement was coeval with a Late Cretaceous compressive regime (Klepeis et al., 2010; Torres Carbonell and Dimieri, 2013), although after peak regional metamorphism, as showed by field and petrographic data.

This work presents a thorough description of the Ushuaia pluton, including field data, petrography, structure, whole-rock and mineral chemistry, and new U–Pb zircon ages. The comprehensive study of the UP provides new insights on the nature and diversification of magmas at different crustal depths, and the mode of emplacement of plutons; with implications on the tectonic evolution of the southernmost Andes. The study of foliations in and around the pluton and contact metamorphism provide time constraints of regional metamorphism and deformation away from the much better studied Cordillera Darwin metamorphic core (see Fig. 1 for location) (e.g. Nelson et al., 1980; Hervé et al., 1981, 2010; Cunningham, 1995; Kohn et al., 1995; Klepeis et al., 2010; Maloney et al., 2011). The relationship between the UP and the Ushuaia Peninsula Andesites is also addressed on the basis of the new data (including a U–Pb age), in order to avoid further misleading interpretations.

2. Regional geology

The Fuegian Batholith was constructed episodically from the latest Jurassic to the Paleogene, as a consequence of subduction along the Pacific trench (Hervé et al., 1984; Suárez et al., 1986; see also Hervé et al., 2007a) (Fig. 1). Early Cretaceous magmatism within the batholith developed concomitant with generation of oceanic-type basalts in the Rocas Verdes marginal basin along the continental margin (Stern and de Wit, 2003; Calderón et al., 2007, 2016). The calc-alkaline Beagle suite (Hervé et al., 1984) formed part of the main arc during the Cretaceous (Fig. 1), with ages between ~117 and 74 Ma (Suárez et al., 1986; Klepeis et al., 2010; McAtamney et al., 2011; Poblete et al., 2016).

Magmatism to the rear of the Cretaceous arc is represented by isolated, small plutons, with a mildly alkaline to monzonitic trend, following the classification of Lameyre and Bowden (1982) and Lameyre (1987). They formed during a potassic magmatic event (Fuegian Potassic Magmatism), during the Late Cretaceous (González Guillot et al., 2009). This suite includes the UP, and represents a constrained magmatic event that lasted < 10 m.y. (González Guillot, 2016). Among the plutons of this suite, the Moat pluton is the most similar to UP, considering mineralogy, relative abundance of lithologies and chemistry, related to its relative position within the rear-arc (González Guillot, 2016). Additionally, several Late Cretaceous subvolcanic intrusions crop out in an area close to the UP (Fig. 1). They consists of plugs of quartz meladiorite, granodiorite, cross-cut by dykes and sills of porphyritic andesite and dacite, all with a high-K, calc-alkaline composition, and without overimposed deformation or metamorphism. They were collectively grouped in the Ushuaia Peninsula Andesites (UPA, González Guillot et al., 2011). The UP and UPA were intruded in Late Jurassic - Early Cretaceous metaturbidites (Fig. 1).

The closure of the Rocas Verdes basin started around ~100 Ma, followed by Late Cretaceous arc-continent collision together with retroarc lithospheric thickening (Calderón et al., 2016), marking the initiation of the Andean orogeny. It was attributed to the flattening of the oceanic slab and was accompanied by cratonward migration of the volcanic front (Stern et al., 1991; Mukasa and Dalziel, 1996; González Guillot et al., 2011). Magmatism ceased in early Maastrichtian and by ca. 60 Ma it resumed backwards, at the outermost (southern) side of the archipelago (Fig. 1, Hervé et al., 1984).

The early orogenic event involved a first stage of contractional deformation due to continental underthrusting below the magmatic arc, with low to moderate pressure (upper to middle crust) and temperature metamorphism and folding prior to ~86 Ma (Nelson et al., 1980; Hervé et al., 1981, 2007b; Cunningham, 1995; Fildani et al., 2003; Menichetti et al., 2008; Klepeis et al., 2010; Maloney et al., 2011; Calderón et al., 2012; Torres Carbonell et al., 2017). Facies of regional metamorphism vary from upper amphibolite in the core of Cordillera Darwin (e.g. Maloney et al., 2011) to prehnite-pumpellyite away from it (e.g. Cao et al., 2018). Fission track thermochronology (Nelson, 1982), $^{40}Ar/^{39}Ar$ cooling ages (Kohn et al., 1995) and monazite U–Pb dating (Maloney et al., 2011) indicate a first pulse of thrusting and rapid exhumation of Cordillera Darwin metamorphic complex between 90 and 70 Ma.

Several authors proposed oblique convergence and a transpressional closure of the Rocas Verdes basin (Cunningham, 1993; Ghiglione and Ramos, 2005; Curtis et al., 2010). Alternative interpretations hold that closure of the marginal basin and Andean deformation was mainly controlled by thrusting, in a compressional regime (Klepeis, 1994; Klepeis et al., 2010; Maloney et al., 2011; Torres Carbonell and Dimieri, 2013).

The basement domain of the orogenic belt became tectonically consolidated by out of sequence (Klepeis et al., 2010; Maloney et al., 2011) or in sequence (Torres Carbonell and Dimieri, 2013) thrusting and crustal thickening and exhumation of hinterland thrusts that could have started as early as 70 Ma (Klepeis et al., 2010), and propagated shortening towards the foreland fold thrust belt during the Paleogene (Álvarez-Marrón et al., 1993; Klepeis, 1994; Olivero and Malumián, 2008; Barbeau et al., 2009; Gombosi et al., 2009, Ghiglione et al., 2010; Torres Carbonell et al., 2017).

Transtensional, left-lateral tectonics took place in the region later, with a major reorganization of lithospheric plates, onset of seafloor spreading in the Scotia sea and transcurrence along the boundary between the South American and Scotia plates. According to Cunningham (1995), transtension could have been initiated along the southern slope of Cordillera Darwin by Late Cretaceous, although later works propose this regime initiated close to the Cretaceous-Tertiary boundary (Mukasa and Dalziel, 1996), or after the Eocene (Gombosi et al., 2009), or even in the Miocene (Klepeis et al., 2010; Maloney et al., 2011, and references therein). In fact, these structures cut 73 Ma old Beagle suite plutons in Cordillera Darwin (Klepeis et al., 2010) and the UP. Deformation shifted later northwards and strike-slip took place along the Magallanes Fagnano-Fault Zone in the Neogene (e.g. Klepeis, 1994; Olivero and Malumián, 2008; Menichetti et al., 2008; Torres Carbonell et al., 2008). This event is characterized by an E-W sinistral strike-slip and oblique-slip faulting overimposed to previous structures.

3. The Ushuaia pluton

The UP is a composite intrusion that crops out immediately east of Ushuaia city, along the northern coast of the Beagle channel (Figs. 1–2). The pluton is intruded in the metaturbidites of the Yahgan Formation, and is almost completely covered by a dense forest (removed in the map of Fig. 2); therefore identification of lithological contacts and rock fabric is often hampered.

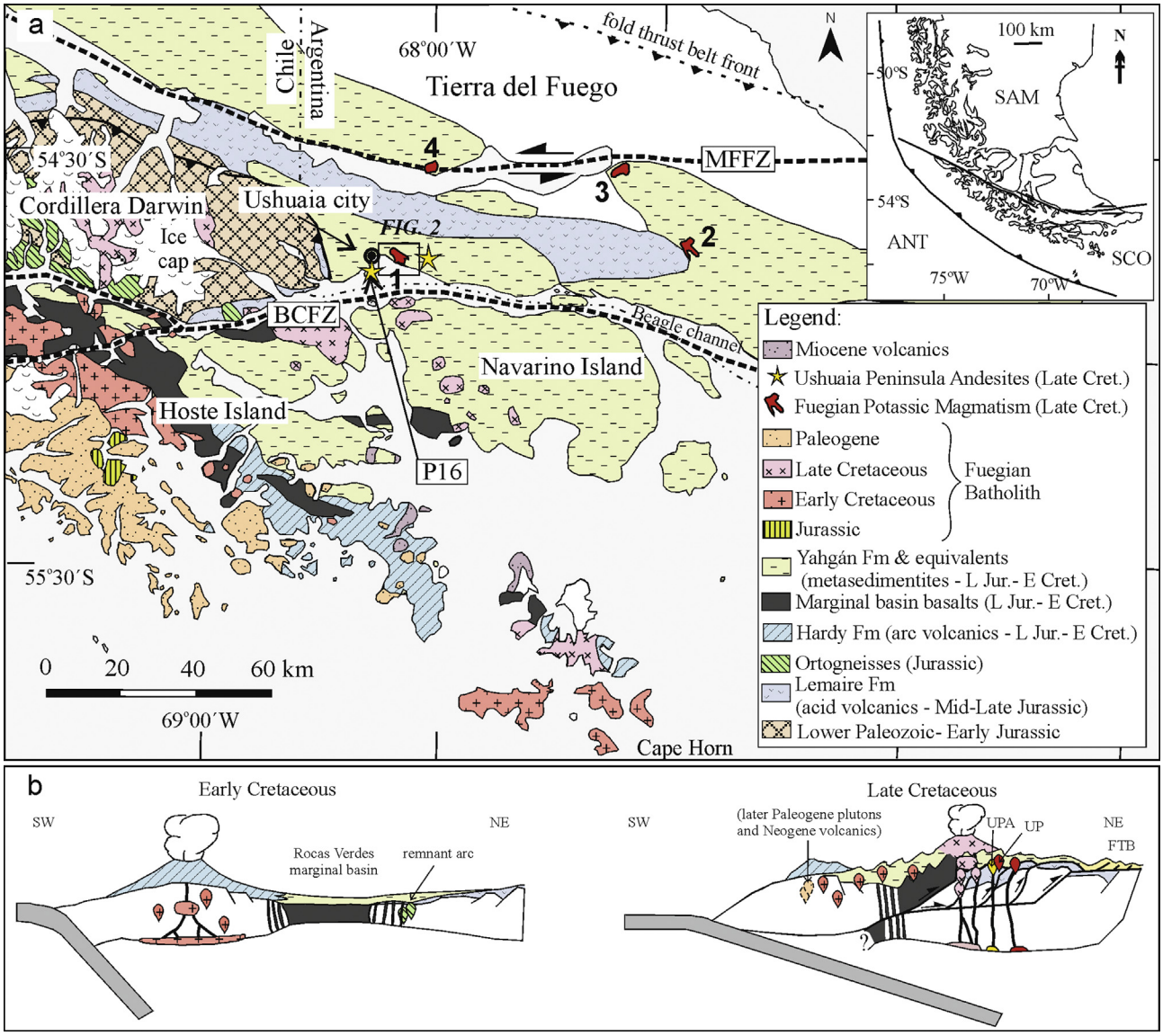

Fig. 1. (a) Regional geologic map of Tierra del Fuego with main geological units indicated in the text. Numbers refer to plutons of the Fuegian Potassic Magmatism: (1) Ushuaia, (2) Moat, (3) Jeu-Jepén, (4) Kranck. Also shown is the location of Fig. 2 and sample P16. The inset shows present plate configuration. BCFZ, Beagle channel fault zone; MFFZ, Magallanes Fagnano fault zone; SCO, Scotia plate; SAM, South American plate; ANT, Antarctic plate. Data sources: Nelson et al. (1980), Hervé et al. (1981), Suárez et al. (1985), SERNAGEOMIN (2003), Olivero and Malumián (2008), González Guillot (2009), Klepeis et al. (2010). (b) Geodynamic sketch from Early to Late Cretaceous (same patterns as in (a), modified from González Guillot (2016)). *(2 column fitting)*.

3.1. General features

On plan view the UP shows a subcircular shape, slightly elongated in NW-SE direction and covers an area of 8.25 km^2 (Fig. 2). The aeromagnetic information (total magnetic field, reduced to pole; SEGEMAR, 1998), however, shows a > 77 km^2, subcircular positive magnetic anomaly, that indicates the pluton is larger underground.

The magnetic anomaly is asymmetric with maximum values over 1200 nT towards its SE extremity, over hornblende pyroxenite outcrops with cumulus magnetite and ilmenite. The geometry of the pluton is partially controlled by regional faults sub-parallel to the shore of the Beagle channel.

Numerical models based on field- and aero-magnetic data show the pluton has a general laccolithic shape, with a root towards the south of the body up to 3.4 or 5 km deep (Menichetti et al., 2007; Peroni et al., 2009, respectively). Both, field data (this Work, Figs. 2–3a) and magnetic modelling (Peroni et al., 2009) indicate the pluton has a general dip towards the SSW, with a thickness over 2.7 km or 2 km, respectively. Contacts with the country rock dip outwards in the SW and W margins, and inward in the N and E margins (Figs. 2–3).

The UP is composed by a wide spectrum of lithologies (Figs. 2–4, Table 1). Two main sections are recognized, with ultramafic-mafic and intermediate lithologies, respectively. The former has a partially concentrical zoned structure with a nucleus of hornblende clinopyroxenites, an outer envelope of hornblendites, followed by a zone of gabbros, diorites and quartz diorites. The second section consists mainly of monzodiorites and quartz monzodiorites that cross-cut the zoned structure (Figs. 2–3a). Each section bears late stage dykelets of different composition, mainly monzodiorite-monzonite in the ultramafic-mafic section, and granite in the intermediate section (Table 1). The zoned structure, petrography and geochemistry of some PGE (platinum group elements), among other features, led González Guillot and Schalamuk (2009) to compare the UP to Alaskan type complexes.

3.1.1. Ultramafic-mafic section

Hornblende pyroxenites crop out in the SE tip of the pluton, with

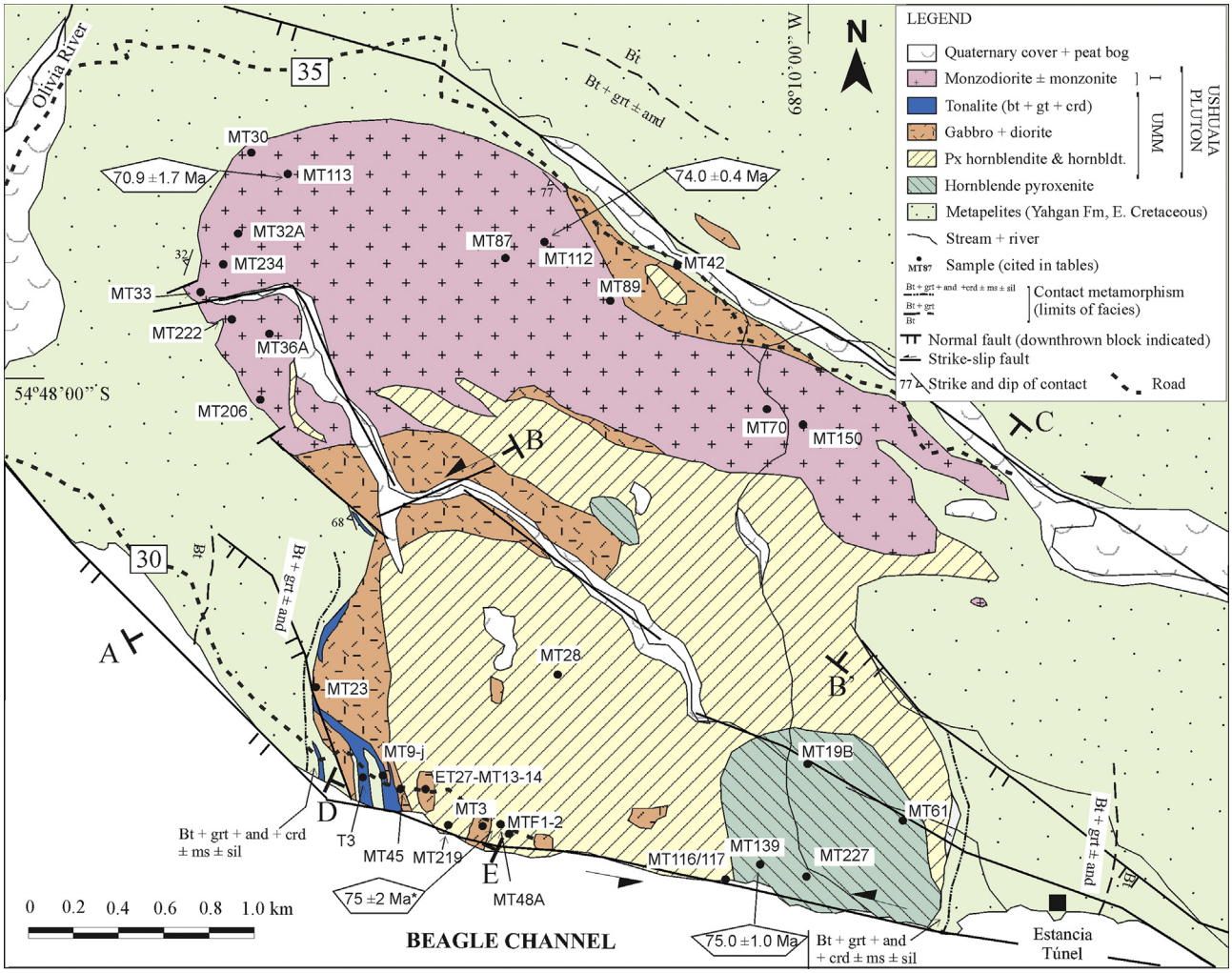

Fig. 2. Geologic map of the Ushuaia pluton (UMM and I are the ultramafic-mafic and intermediate sections). The location of the samples referred to in Tables 1–3 and Section 4 is indicated, as well as the location of profiles of Fig. 3a–b. Contacts are drawn as sharp lines for clarity, but boundaries between lithologies are gradational. Ages are form this work and Barbeau et al. (2009*). Late stage monzonite, granodiorite and granite dykelets are too thin to be represented in this map. *(2 column fitting)*.

minor exposures towards the centre, enveloped by pyroxene hornblendites and hornblendites and finally gabbro/diorite (and quartz gabbro/diorite, Fig. 2). There is a transitional passage from hornblende pyroxenites through pyroxene hornblendites to pure hornblendites, then an outer zone of mingled hornblendite and gabbro/diorite (Fig. 3b, see also Fig. 6a), accompanied by reduction in grain size, and then diorite/gabbro (Fig. 3b). Metre-scale subvertical layering between ultramafic rocks and gabbro (Fig. 5), and centimetre-scale layering between gabbro/diorite layers with variable orientations are observed. The mafic layers show igneous foliation parallel to layer boundaries. Irregular microgranular synmagmatic dykes of gabbro and melagabbro up to 3–20 cm thick are common in ultramafic rocks, as well as pockets and segregations of coarse grained to pegmatitic gabbro to monzogabbro/monzodiorite (Fig. 6b).

Dykes of gabbro/diorite into gabbro/diorite with different mafic mineral content or texture are common, with diffuse contacts on the mm scale, indicating multiple injections prior to complete crystallization of the former batches (Fig. 3b). The contacts between gabbros and hornblendites are many times transitional in a ~1–2 m wide zone.

Late stage rectilinear or anastomosed dykelets and segregations (1–0.01 m thick) consist of monzodiorite, monzonite and quartz monzonite (Fig. 4, Table 1). They cross-cut the ultramafic rocks and gabbro/diorite. In the ultramafic rocks these lithologies occur also as breccia infill (Figs. 3b and 6c-d). Hereafter, we refer to these late stage rocks exclusively as dykelets to distinguish them from the gabbro/monzogabbro/monzodiorite segregations and pockets aforementioned.

At the SW contact of the pluton several metre-scale apophyses of tonalite crop out separated each other by metasedimentary septa (Figs. 2 and 3b). They consist of elongated strips sub-parallel to the pluton margin, intercalated between country metapelites and underlying gabbro/diorite. They bear abundant metasedimentary enclaves with diffuse contacts, and are cut by thin dykelets of more leucocratic tonalite-granodiorite (Fig. 4, Table 1). The contact between the tonalite and gabbro/diorite is gradational.

3.1.2. Intermediate section

The monzodiorites, quartz monzodiorites and minor monzonites form a main body towards the north of the pluton, with a NW-SE elongation (Fig. 2). Contacts between these rocks and diorite/gabbro of the ultramafic-mafic section are transitional. There occurs fine-scale igneous layering among all these lithologies (Fig. 7a, see below). Moreover, thin dykes (10–30 cm thick) of fine-grained diorite/gabbro within the monzodiorites dismember and mingle (Fig. 7b), or form dispersed rounded autoliths elsewhere. Contrarily, autoliths of hornblende pyroxenite, hornblendite and pegmatitic gabbro pockets in the monzodiorites are angular and coarse-grained without chilled margins; and metre-scale dykes of monzodiorite cut pyroxene hornblendites and their gabbro/monzogabbro segregations (Fig. 7c).

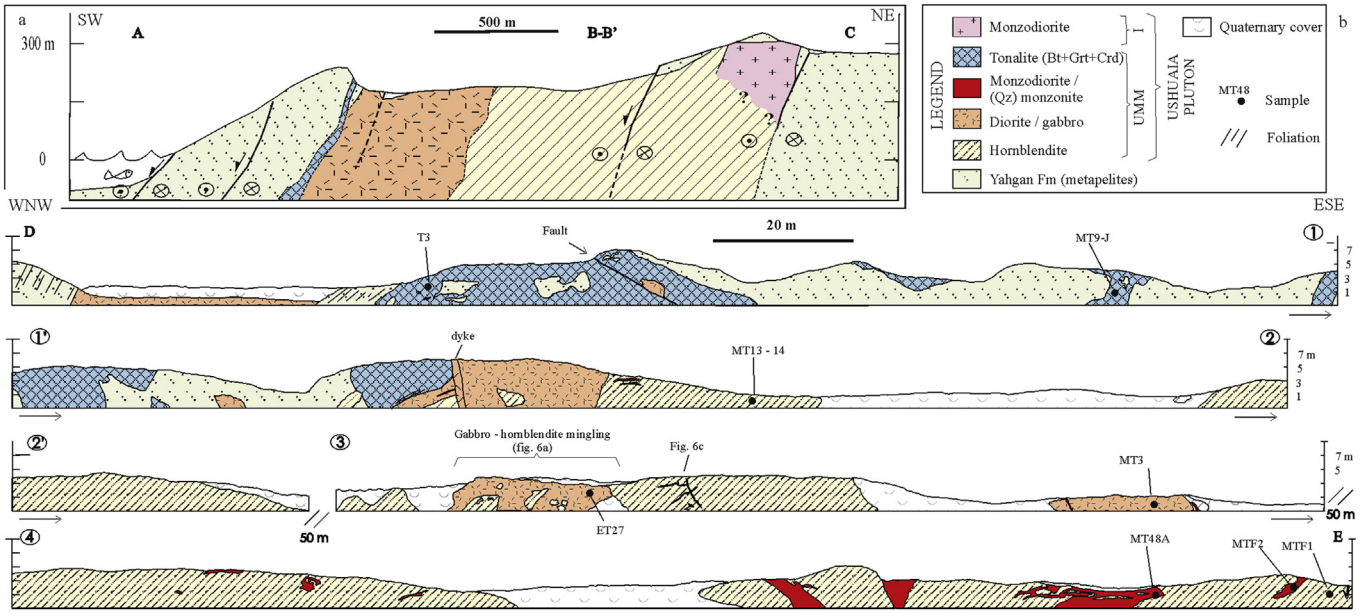

Fig. 3. Profiles across UP (location in Fig. 2). (a) Schematic SW-NE cross section (A–C) with vertical exaggeration (UMM and I refer to ultramafic-mafic and intermediate sections). (b) Geologic profile D-E (split in 4 sections) along 30 Provincial Road. Two sections of 50 m without outcrop were omitted. The location of some samples referred to in Tables 1–3 is indicated. *(1.5 column fitting)*.

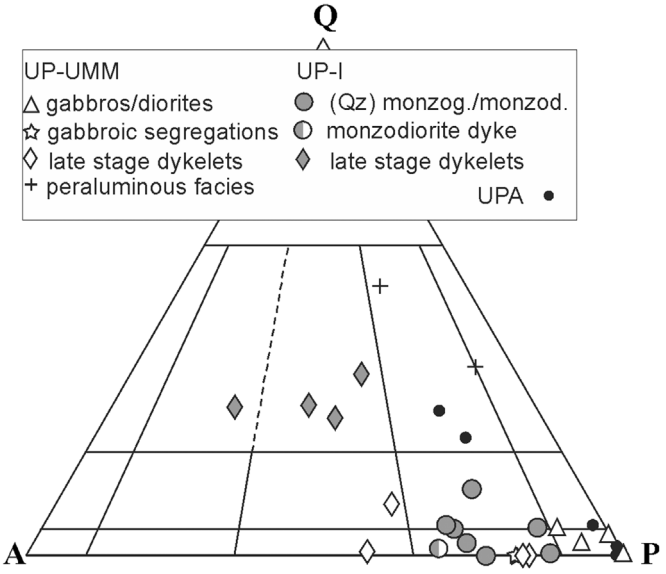

Fig. 4. QAP diagram for UP and the Ushuaia Peninsula Andesites (UPA; González Guillot et al., 2011). UMM and I: ultramafic-mafic and intermediate sections, respectively. The gabbroic segregations occur in ultramafic rocks. The monzodiorite dyke in the intermediate section (sample MT116) cross cuts pyroxene hornblendite and its gabbroic segregations (see Fig. 7d). *(single column fitting)*.

Late stage dykelets and segregations (1–10 cm thick) consist of granite and minor quartz monzonite, with sharp or diffuse contacts (Figs. 4 and 7d, Table 1). Hereafter, we also refer to these late stage rocks as dykelets.

The quartz monzodiorites occur close to the contacts with country rock, and bear diffuse enclaves of metapelite, from which quartz rich veins emanate (Fig. 7e).

10–20 cm thick Hbl-phyric lamprophyre dykes cut all rocks in both sections. Those hosted in monzodiorites (intermediate section) show back-veining structures with the host (Fig. 7f); whereas no such a relation was seen in the ultramafic-mafic section.

3.2. Petrography

Hornblende pyroxenites are dark coloured, coarse grained[3] rocks composed of clinopyroxene (diopside), hornblende, apatite, biotite-phlogopite, magnetite, ilmenite, ferro-spinel (pleonaste) and rare plagioclase. Textures are cumular, with cumulus pyroxene, apatite, hornblende and opaque minerals, with polygonal contacts, and additional, poikilitic hornblende, biotite-phlogopite, opaque minerals and occasional plagioclase as intercumulus material (Fig. 8a). The polygonal contacts suggest textural modification at subsolidus state. The pyroxene shows no zonation and is variably replaced by patchy hornblende. Intercumulus hornblende and rims on cumulus hornblende are slightly darker than cumulus hornblende cores. No olivine or orthopyroxene occur in the UP or the other plutons of the suite (González Guillot et al., 2009). Opaque minerals form 1–5 cm long polycrystalline aggregates that reach up to 20% in volume in the centre of the hornblende pyroxenite body. The textures are described in González Guillot and Schalamuk (2009).

Hornblendites and pyroxene hornblendites are coarse grained (coarser than hornblende pyroxenites), with hornblende crystals up to 7 cm long; or medium grained where they are in contact or mingled with gabbro or diorite. The crystals are arranged generally in a random fashion, although some samples show crystal orientation. Textures are also cumular. Clinopyroxene, opaque minerals and biotite-phlogopite are scarcer than in hornblende pyroxenites, and ferro-spinel is absent. Plagioclase, apatite, sphene and primary epidote are minor constituents.

The synmagmatic gabbro and melagabbro dykes in the ultramafic rocks are microgranular to porphyritic, with scarce hornblende ± clinopyroxene and biotite primocrysts in a fine grained groundmass of plagioclase, hornblende, pyroxene, biotite, apatite, opaque minerals and zircon. Crystals are oriented subparallel to dyke walls, defining a magmatic foliation with alternating plagioclase and hornblende rich bands. On the other hand, the pegmatitic gabbro-monzogabbro/monzodiorite pockets and segregations are composed of plagioclase, hornblende, apatite, sphene, opaque minerals, and occasional biotite and K-

[3] Granulometric boundaries of Hibbard (1995) are used in this work.

Table 1
Modal composition of Ushuaia pluton.

Sample	Lithol.	Kfs	Pl	Qz	Hbl	Cpx	Bt	Spn	Ap	Opq	Zrn	Ep	Other*	TOT	M'%	Q	A	P
Ultramafic-mafic section																		
Ultramafic rocks																		
MT61	hbl pxt	–	–	–	29.7	35.0	–	–	18.2	17.1	–	–	–	100.0	82	0	0	0
MTF1	hbt	–	–	–	68.8	–	–	–	0.6	7.7	–	0.4	22.5	100.0	99	0	0	0
MT13	hbt	–	2.1	–	95.2	–	–	–	0.9	–	–	–	1.8	100.0	97	0	0	0
MT28	hbt	–	–	–	90.1	0.2	0.2	0.2	7.4	1.3	–	0.2	0.5	100.0	93	0	0	0
Gabbroic segregations in ultramafic rocks (some with pegmatitic texture)																		
MT117	mzd/mzg (seg)	14.2	65.4	–	12.6	3.1	2.9	1.0	tr	tr	tr	–	0.7	100.0	20	0	18	82
MT227	mzd/mzg (seg)	15.2	78.3	–	1.8	1.1	–	0.8	0.2	–	0.1	–	2.5	100.0	6	0	16	84
Gabbros/diorites																		
MT23	dio	3.5	35.9	2.2	57.7	–	0.2	0.2	0.4	–	–	–	–	100.0	58	5	8	86
ET27	gab	–	69.2	0.1	27.3	–	–	0.7	0.5	0.7	0.2	0.1	1.1	100.0	30	0	0	100
MT42	dio	3.9	60.5	1.5	31.9	tr	–	1.0	0.3	0.8	tr	–	–	100.0	34	2	6	92
MT45	dio	0.4	66.9	2.6	5.3	–	15.8	–	1.2	5.0	–	–	2.7	100.0	29	4	1	96
Late stage leucocratic dykelets																		
MTF2	mzn (dlt)	42.1	56.7	0.4	0.2	–	–	0.4	tr	–	0.2	–	–	100.0	1	0	42	57
MT13	mzd (dlt)	16.3	81.4	–	1.0	–	–	0.1	tr	0.5	0.3	–	0.3	100.0	1	0	17	83
MT48-A	qz mzn (dlt)	33.2	55.6	10.0	0.6	–	–	0.1	tr	0.5	tr	–	–	100.0	1	10	34	56
MT219	mzd (dlt)	14.3	77.1	0.1	0.4	–	–	tr	tr	–	tr	–	8.0	100.0	0	0	16	84
Peraluminous facies																		
MT9-J	ton	4.9	46.1	29.7	–	–	14.0	–	tr	0.5	–	–	4.8	100.0	19	37	6	57
T3	grd (dlt)	13.5	31.5	48.7	–	–	–	–	–	–	tr	–	6.3	100.0	6	52	14	34
Intermediate section																		
(Qz) Monzogabbros/monzodiorites																		
MT30	mzd	19.4	51.2	3.8	18.6	–	–	1.6	0.8	–	tr	–	4.7	100.0	25	5	26	69
MT32-A	qz mzd/mzg	15.7	56.6	10.8	15.2	–	–	0.7	0.2	0.5	0.2	tr	0.1	100.0	17	13	19	68
MT36-A	qz mzd/mzg	19.5	49.1	4.4	23.0	tr	–	1.4	0.9	0.9	0.1	0.1	0.7	100.0	26	6	27	67
MT70	mzd/mzg	7.8	56.1	3.8	26.1	2.7	–	0.7	0.8	0.3	–	–	1.6	100.0	31	6	12	83
MT87	mzd	18.3	60.4	–	13.7	4.2	–	0.8	0.4	2.1	tr	–	0.1	100.0	21	0	23	77
MT89-drk	mzd	5.5	41.1	0.2	45.3	5.2	0.8	1.1	0.4	0.1	0.1	–	0.2	100.0	53	0	12	88
MT89-lgt	mzd	17.9	52.1	1.6	24.4	0.4	–	1.2	0.7	1.4	0.1	–	0.1	100.0	28	2	25	73
MT116	mzd (d)	28.3	64.7	1.4	0.1	3.0	–	0.6	tr	1.0	0.4	–	0.5	100.0	5	1	30	69
Late stage leucocratic dykelets																		
MT33	mzgrt (dlt)	38.2	32.5	28.9	–	–	–	–	–	–	tr	–	0.5	100.0	0	29	38	33
MT150	mzgrt (dlt)	25.9	38.2	34.9	0.3	–	tr	tr	–	tr	0.1	–	0.6	100.0	1	35	26	39
MT206	mzgrt (dlt)	34.8	38.2	26.5	–	–	–	–	–	–	tr	–	0.6	100.0	1	27	35	38
MT222	sygrt (dlt)	50.7	20.4	28.5	0.4	tr	–	tr	–	tr	tr	–	–	100.0	0	29	51	20

* Other is alteration of mafic minerals; except in MT9-J: 1.2% garnet, 0.1% muscovite plus altered cordierite. InT3 other is: 0.2% garnet, 0.6% vesuvianite, 4.4% muscovite. In MT32-A other is: allanite, and in ET27 is zeolite. Abbrebiations: hbl pxt: hornblende pyroxenite, hbt: hornblendite, dio: diorite, (qz) mzd/mzg: (quartz) monzodiorite/monzogabbro, mzn: monzonite, ton: tonalite, grd: granodiorite, mzgrt: monzogranite; (d): dyke, dlt: dykelet; drk-lgt: dark and light layers in layered monzodiorite; Kfs: K-feldspar, Pl: plagioclase, Qz: quartz, Hbl: hornblende, Cpx: clinopyroxene, Bt: biotite, Spn: sphene, Ap: apatite, Opq: opaques, Zrn: zircon, Ep: epidote; M'%: color index (Hbl + Cpx + Bt + Spn + Opq + Zrn + Ep + Other), QAP: parameters of QAP diagram, tr: traces.
Modal compositions have been determined by grid counting (ca. 1000 points per thin section).

feldspar (some of them contain pyroxene). Commonly, crystals are oriented parallel to the walls (Fig. 6b). Hornblende has high to low integrity (c.f. Hibbard, 1995), the last case results in abundant inclusions of plagioclase laths in a subofitic relation. The plagioclase shows intense sericitization, while interstitial K-feldspar is clear.

Gabbros, diorites, monzodiorites, quartz diorites and quartz monzodiorites (both sections) are generally medium grained. Mafic mineral content is variable and some specimens are leuco- or melanocratic (Table 1). The centimetre scale layering mentioned above is given by alternating dark and light layers, due to differential abundance of mafic and felsic minerals and grain size. Elongated, euhedral crystals are oriented parallel to layers defining an igneous foliation (Fig. 8b). The textures are granular hypidiomorphic and trachytic.

The modal composition in gabbros and diorites (ultramafic-mafic section) is plagioclase, hornblende, magnetite, ilmenite, apatite, sphene, zircon, and occasional K-feldspar and quartz. Diopside and/or biotite may appear along with hornblende (Table 1). The order of crystallization is given by early appearance of zoned, euhedral plagioclase, followed by pyroxene (if present), and then hornblende + more sodic and finer plagioclase grains or rims on former plagioclase crystals. Sphene, apatite and zircon appear before hornblende crystallization (zircon usually appears included in plagioclase cores). Late interstitial phases are K-feldspar ± quartz.

Monzodiorites and quartz monzodiorites (intermediate section) are composed of the same minerals (Table 1) with the same order of crystallization as in gabbros/diorites, with the exception that interstitial K-feldspar ± quartz are more abundant, and may develop 1–2 cm to 10–20 cm thick lenses rich in K-feldspar, parallel to igneous foliation (Fig. 8c). The layers are monzonitic in composition and some contain 1–4 cm megacrysts of K-feldspar. Additionally, K-feldspar (without internal deformation) replaces early-formed plagioclase, which develops a rim of myrmekite on the plagioclase (Fig. 8d). According to Drescher-Kaden (1948) the myrmekite forms with the assistance of K and Si bearing fluids (see review in Rong and Wang, 2016).

The late stage leucocratic dykelets of both sections have granular to aplitic texture. The mineral assemblage is subhedral plagioclase, microperthitic K-feldspar, minor hornblende, apatite, sphene, zircon, and variable amounts of quartz. Scarce clinopyroxene and biotite appear in some dykelets of the intermediate section (Table 1). As mentioned above, in the ultramafic-mafic section they consist of monzodiorite and (quartz) monzonite, with ratios of Kfs:Qz of 134–3:1, and Pl:Kfs ~3.3:1; whereas in the intermediate section their composition is mainly granite, with ratios of Kfs:Qz of ~1.3:1 and Pl:Kfs of ~1:1. Some dykelets in the ultramafic-mafic section are zoned, with a monzonitic central part and megacrysts of K-feldspar towards the walls (Fig. 8e).

All the late stage leucocratic dykelets show evidence of deformation, while the host rock is undeformed. Subgrain development and recrystallization around or along fractures in K-feldspar and plagioclase

Table 2
Average mineral composition of silicates and oxides of the Ushuaia pluton.

Phase	Plagioclase						K-feldspar			Pyroxene					Amphibole						
Label	MT89						MT89			MT61		MT89			MT61		MT89		ET1[a]	ET2[a]	U23[a]
Lithol.	mzd-drk			mzd-lgt			mzd-drk	mzd-lgt		hbl pxt		mzd-drk	mzd-lgt		hbl pxt		mzd-drk	mzd-lgt	hbt	hbt	hbt
Texture	euh	small	inst	euh	small	inst	inst	inst		core	rim				cum	i-cum					
(n)	(2)	(3)	(2)	(3)	(4)	(5)	(1)	(6)		(12)	(4)	(2)	(3)		(6)	(2)	(2)	(6)	(5)	(8)	(2)
SiO_2	55.34	59.87	59.47	56.33	59.06	64.50	64.06	63.94	SiO_2	48.75	48.26	52.23	52.52	SiO_2	40.13	40.01	46.42	43.59	40.26	40.94	41.26
TiO_2	0.02	0.01	0.02	0.03	0.02	0.01	0.02	0.01	TiO_2	0.77	0.83	0.10	0.16	TiO_2	1.91	1.88	1.17	1.20	1.94	1.84	1.77
Al_2O_3	27.60	24.72	25.09	26.65	25.07	21.70	18.37	18.35	Al_2O_3	4.84	4.99	0.99	1.35	Al_2O_3	13.43	14.08	9.46	9.04	12.88	11.43	12.01
Cr_2O_3	–	–	–	–	–	–	–	–	Cr_2O_3	0.03	0.03	0.04	0.01	Cr_2O_3	0.03	0.04	0.03	0.04	0.00	0.01	0.00
Fe_2O_3(c)	0.13	0.21	0.17	0.17	0.20	0.13	0.05	0.10	Fe_2O_3(c)	4.62	5.56	2.92	2.77	Fe_2O_3(c)	3.98	3.07	7.32	5.36	5.26	5.34	4.72
FeO(c)	–	–	–	–	–	–	–	–	FeO(c)	3.31	2.61	4.70	6.67	FeO(c)	7.51	7.14	9.68	12.22	11.48	12.81	11.09
MnO	–	–	–	–	–	–	–	–	MnO	0.20	0.20	0.61	0.85	MnO	0.18	0.15	0.55	0.55	0.45	0.42	0.28
MgO	0.00	0.01	0.01	0.00	0.00	0.00	0.00	0.00	MgO	13.15	13.13	14.11	12.34	MgO	13.76	13.98	12.66	11.04	10.28	9.96	11.32
CaO	10.12	6.60	6.96	8.97	7.02	5.15	0.00	0.05	CaO	23.83	23.99	23.37	22.98	CaO	12.38	12.60	11.95	11.78	11.45	11.31	11.62
Na_2O	5.54	7.61	7.46	5.97	7.34	8.65	0.44	1.08	Na_2O	0.33	0.32	0.46	0.22	Na_2O	2.06	1.93	1.35	1.32	1.99	1.95	2.02
K_2O	0.12	0.21	0.19	0.17	0.17	0.23	14.60	13.99	K_2O	0.00	0.01	0.00	0.02	K_2O	1.53	1.40	0.98	1.08	1.25	1.39	1.30
NiO	–	–	–	–	–	–	–	–	NiO	–	–	–	–	NiO	0.03	0.02	0.09	0.02	–	–	–
H_2O(c)	–	–	–	–	–	–	–	–	H_2O(c)	–	–	–	–	H_2O(c)	2.02	2.02	2.11	1.99	–	–	–
Sum	98.85	99.24	99.35	98.30	98.87	100.39	97.54	97.52	Sum	99.83	99.91	99.51	99.89	Sum	98.81	98.28	103.73	99.23	97.23	97.40	97.37
Ab	49.39	66.78	65.28	54.09	64.77	74.58	4.41	10.45	Wo(Ca)	49.52	49.61	47.53	47.93	Mg#	0.77	0.78	0.70	0.62	0.62	0.58	0.65
An	49.95	32.02	33.62	44.88	34.24	24.15	0.00	0.26	En (Mg)	38.04	37.78	39.80	35.77	Leake	MH	P	MHb	MHb	MH	MH	MH
Or	0.66	1.20	1.11	1.02	0.99	1.27	95.59	89.29	Fs(Fe^{2+} + Mn)	12.44	12.61	12.68	16.30								
									Mg#	0.88	0.90	0.84	0.74								

	Magnetite			Ilmenite					Ferro-Spinel		
	MT19-B	MTF1		MT19-B		MTF1			MT19-B		
	hbl pxt	hbt		hbl pxt		hbt			hbl pxt		
				cryst	ex-mgt	cryst	ex-mgt		ex-il	ex-mgt	cryst
	(8)	(3)		(6)	(4)	(2)	(3)		(2)	(3)	(3)
SiO_2	0.20	–	SiO_2	0.12	0.07	0.22	0.11	SiO_2	0.17	0.45	0.16
TiO_2	0.79	0.15	TiO_2	52.83	50.77	49.07	49.35	TiO_2	0.37	0.18	0.15
Al_2O_3	1.33	0.55	Al_2O_3	0.06	2.52	0.26	0.04	Al_2O_3	64.15	65.10	62.31
Cr_2O_3	0.38	0.10	Cr_2O_3	0.09	0.18	0.03	0.04	Cr_2O_3	0.70	0.41	0.40
Fe_2O_3(c)	65.65	67.64	Fe_2O_3(c)	7.34	6.44	5.57	5.91	Fe_2O_3(c)	2.95	3.74	4.88
FeO(c)	31.21	31.27	FeO(c)	27.97	25.54	36.96	38.59	FeO(c)	9.78	7.67	12.00
MnO	0.04	0.02	MnO	2.10	2.88	6.97	5.52	MnO	0.14	0.11	0.14
MgO	0.70	0.03	MgO	9.83	9.67	0.13	0.09	MgO	21.31	23.21	19.70
CaO	–	–	CaO	0.01	0.01	0.08	0.11	CaO	–	–	–
Na_2O	–	–	Na_2O	–	–	–	–	Na_2O	–	–	–
K_2O	–	–	K_2O	–	–	–	–	K_2O	–	–	–
NiO	0.08	0.03	NiO	0.02	0.04	0.04	0.01	NiO	0.02	0.04	0.06
H_2O(c)	–	–	H_2O(c)	–	–	–	–	H_2O(c)	–	–	–
Sum	100.37	99.80	Sum	100.37	98.03	99.31	99.79	Sum	99.41	100.45	98.63
XCr	51.98	41.10	Ilmenite	57.83	52.13	79.04	82.08	XCr	0.73	0.42	0.42
XFe^{2+}	96.24	99.85	Geikielite	31.14	35.76	0.48	0.37	XFe^{2+}	20.48	15.64	25.89

(*continued on next page*)

Table 2 (*continued*)

	Magnetite			Ilmenite				Ferro-Spinel			
	MT19-B	MTF1		MT19-B		MTF1		MT19-B			
	hbl pxt	hbt		hbl pxt		hbt		hbl pxt			
				cryst	ex-mgt	cryst	ex-mgt	ex-il	ex-mgt	cryst	
	(8)	(3)		(6)	(4)	(2)	(3)	(2)	(3)	(3)	
YFe^{3+}	96.46	98.59	Pyrophan.	4.39	6.04	15.14	11.91	YFe^{3+} 2.83	3.52	4.76	
			Hematite	6.64	6.07	5.34	5.65				

References: mzd: monzodiorite (layered, with dark (drk) and light (lgt) layers); hbl pxt: hornblende pyroxenite; hbt: hornblendite; euh: euhedral crystal; small: small ehuedral crystal and rim on euh; inst: interstitial; cum: cumulus; i-cum: intercumulus and rim of cum; cryst: crystal intergrown with magnetite; ex-mgt and ex-il: exsolution lamella in magnetite or ilmenite, respectively. Mg#: $Mg/(Mg + Fe^{2+})$, XCr: $100*Cr/(Cr + Al)$, XFe^{2+}: $100*Fe^{2+}/(Mg + Fe^{2+})$, YFe^{3+}: $100*Fe^{3+}/(Fe^{3+} + Cr + Al)$. Amphibole nomenclature according to Leake et al. (1997), MH: magnesiohastingsite, MHb: magnesiohornblende, P: pargasite. [a] from Acevedo (1996). MT61, MT19-B, MTF1, ET1, ET2, U23: ultramafic-mafic section. MT89: intermediate section.

grains are typical (Fig. 8f). Additionally, the larger crystals show undulatory extinction and bending. Later brittle deformation consists of brecciation by hydrothermal fluids that deposited epidote. This is a common feature of late stage, leucocratic dykelets in all potassic plutons of the Fuegian Andes.

The tonalite contains an S-type paragenesis: biotite, garnet ± muscovite and cordierite (Table 1). At mesoscale, biotite and garnet are more abundant in schlieren around metasedimentary enclaves, and at outcrop scale these phases, along with quartz progressively disappear as hornblende appears gradually towards the contacts with diorite/gabbro and away from the country rock. The thin leucocratic dykelets of tonalite-granodiorite within the tonalities contain garnet, muscovite and vesuvianite (?) (Table 1).

It is worth mentioning that metamorphism and deformation is absent in all the lithologies described above, including foliated rocks. The only exceptions are the late stage leucocratic dykelets aforementioned, and scattered rocks along the pluton margin, which show minor deformation (see Section 6). The hornblende and spinel grains analyzed by microprobe (see next section) show igneous affinities (c.f. Leake, 1965; Barnes and Roeder, 2001).

3.3. Mineral chemistry

Electron microprobe analyses of silicate minerals were carried out in a hornblende pyroxenite (MT61, ultramafic-mafic section) and a layered monzodiorite (MT89, intermediate section) (Table 1); opaque minerals were analyzed in hornblende pyroxenites and hornblendites (ultramafic-mafic section). See location of samples in Fig. 2. Acevedo (1996) also reports amphibole compositions from hornblendites. Results are summarized in Table 2. Since data from other lithologies of UP are lacking, we additionally include clinopyroxene and hornblende compositions (González Guillot, 2009) from ultramafic and mafic rocks of the Moat pluton (same suite as the UP, González Guillot et al., 2009). The rocks are compositionally and texturally equivalent to the ultramafic-mafic section of UP: a clinopyroxene hornblendite, two gabbro segregations (one with pegmatitic texture) and a microgranular gabbro dyke; the gabbros are hosted in hornblende pyroxenites and hornblendites. The analytical procedure is given in the appendix, and complete results of pyroxene and hornblende compositions from UP and Moat pluton are given in a supplementary file (Table S1).

Larger plagioclase crystals in the monzodiorite have labradorite to high-Ca andesine core compositions (average An_{50} and An_{45} in the Hbl and Plg rich layers, respectively). External zones in these and smaller crystals are more sodic (An_{34-31}, range for both layers). Late anhedral plagioclase and K-feldspar have compositions of An_{34-15} and Or_{96-87}, respectively (range for both layers).

The pyroxene is diopside in all cases (according to Morimoto, 1989), with almost constant core to rim compositions. In the hornblende pyroxenite (MT61) only a slight variability in SiO_2, TiO_2 and Al_2O_3 was detected. From core to rim SiO_2 decreases from 48.75% to 48.26%, and TiO_2 and Al_2O_3 increase from 0.77% to 0.83% and from 4.84% to 4.99%, respectively, at almost constant Mg#. Jagoutz et al. (2007) found that 1–2% decrease in Al_2O_3 from core to rim in natural clinopyroxene, crystallized from hydrous calc-alkaline magmas at 5–7 kbar, and a slight increase in Mg# indicate subsolidus reequilibration; therefore, the pyroxene in the UP appears to have undergone no significant chemical reequilibration. Average compositions are $Wo_{49.5}En_{38.0}Fs_{12.5}$, Mg# 0.88 in the hornblende pyroxenite, and $Wo_{47.9}En_{35.8}Fs_{16.3}$, Mg# 0.75 in the monzodiorite. Cr content is low, with maximum of 411 ppm in the Hbl pyroxenite.

Moat pluton pyroxenes are also diopside, with compositions $Wo_{49.4}En_{38.0}Fs_{12.6}$, Mg# 0.89 in the pyroxene hornblendite, $Wo_{49.0}En_{38.1}Fs_{12.9}$, Mg# 0.86 in the gabbro segregations, and $Wo_{48.9}En_{35.6}Fs_{15.5}$, Mg# 0.87 in the microgranular gabbro. The Al_2O_3 content in the pyroxene decreases from 4.97% in the pyroxene hornblendite to 3.14–2.47 in the gabbros. The Cr content is also low, with

Table 3
Major, trace and rare earth element composition of Ushuaia pluton.

Section	Ultramafic-mafic					Intermediate			
Sample	MT14	MT3	ET27	MT9-J	MTF2b	MT87	MT70	MT32-A	MT116
Lithol.	gabbro[1]	gabbro	gabbro	ton	mzn[2]	mzd	mzd	qtz mzd	mzd[3]
Major elements, Wt%									
SiO_2	44.87	47.68	50.76	57.51	61.79	53.69	54.68	59.62	63.05
TiO_2	1.29	0.70	0.90	0.79	0.29	0.69	0.71	0.60	0.17
Al_2O_3	14.01	20.99	19.80	18.93	18.00	19.35	16.76	17.35	19.00
Fe_2O_3t	13.46	8.85	8.82	7.57	4.85	7.00	7.83	5.78	2.61
MgO	7.01	2.85	2.95	2.88	2.78	2.06	3.20	1.72	0.32
MnO	0.20	0.20	0.16	0.17	0.02	0.21	0.19	0.17	0.08
CaO	10.86	10.82	7.02	4.52	0.25	7.80	7.90	5.95	1.73
Na_2O	2.10	4.03	4.55	3.35	0.41	4.42	3.37	3.94	6.50
K_2O	3.73	1.30	2.60	1.50	8.04	2.99	3.27	3.20	5.62
P_2O_5	0.39	0.47	0.46	0.19	0.05	0.41	0.40	0.30	0.04
LOI	1.90	1.80	1.80	2.50	3.3	1.00	1.40	1.10	0.5
Sum	99.82	99.69	99.82	99.91	99.78	99.62	99.71	99.73	99.62
K_2O/Na_2O	1.78	0.32	0.57	0.45	19.61	0.68	0.97	0.81	0.86
DI	35.62	39.25	53.72	56.05	75.08	55.55	53.21	63.83	88.37
Mg#	0.51	0.39	0.40	0.43	0.53	0.37	0.45	0.37	0.20
Trace elements, ppm									
Cr	6.84	6.84	20.53	68.42	–	47.89	82.11	95.79	–
Ni	28.00	7.00	5.00	33.00	–	13.00	23.00	12.00	–
Ba	1695.6	404.8	973.3	370.30	665.0	877.2	739.0	602.5	1907.0
Hf	1.70	1.30	5.20	3.20	9.00	3.50	2.70	4.20	4.20
Nb	1.50	1.70	9.90	7.00	14.20	9.10	5.30	8.40	5.50
Rb	77.10	27.60	66.40	45.20	422.40	64.80	99.10	105.60	114.10
Pb	2.60	2.20	4.20	9.60	–	–	–	–	–
Sr	523.4	2833.2	1128.5	687.4	29.3	2072.4	1458.1	1233.2	1180.7
Ta	0.20	0.20	0.90	0.50	1.10	0.70	0.40	0.50	0.30
Th	2.80	1.10	5.40	10.10	18.40	6.20	11.00	15.20	8.00
U	0.90	0.20	2.30	3.70	4.30	1.60	3.30	4.60	1.90
V	406.0	251.0	209.0	175.0	11.00	169.0	216.0	118.0	44.00
Zr	44.50	25.00	192.00	122.10	313.70	147.50	104.40	165.80	164.00
Y	16.30	19.00	39.70	29.70	28.10	28.50	20.80	24.90	10.50
Rare Earth Elements, ppm									
La	11.50	28.00	30.80	24.40	34.40	35.70	26.80	30.90	22.70
Ce	30.00	66.60	81.00	59.20	75.60	86.20	61.60	70.30	39.70
Pr	4.29	8.39	10.90	5.97	8.45	10.46	7.51	8.27	4.01
Nd	20.20	34.70	47.40	23.70	32.30	42.40	30.80	34.40	14.20
Sm	5.30	7.30	9.90	5.40	6.11	8.37	6.31	6.48	2.40
Eu	1.56	2.33	2.75	1.39	0.81	2.13	1.60	1.65	0.70
Gd	4.19	5.86	8.69	4.94	5.77	6.59	4.99	5.11	1.94
Tb	0.67	0.76	1.38	0.87	0.86	1.04	0.76	0.81	0.25
Dy	3.56	3.92	7.36	5.30	5.91	4.91	3.62	4.22	1.53
Ho	0.60	0.66	1.38	1.05	1.07	0.90	0.66	0.76	0.30
Er	1.56	1.66	4.08	3.09	2.98	2.77	2.04	2.42	0.94
Tm	0.23	0.25	0.65	0.53	0.47	0.38	0.27	0.35	0.17
Yb	1.36	1.49	3.65	3.24	3.34	2.64	1.98	2.47	1.21
Lu	0.19	0.23	0.54	0.50	0.57	0.38	0.30	0.37	0.20
$(La/Yb)_N$	6.07	13.48	6.05	5.40	7.39	9.70	9.71	8.97	13.46
Eu/Eu*	1.01	1.09	0.91	0.82	0.42	0.88	0.87	0.88	0.99

[1] Sinmagmatic dyke in hornblendite. [2] Dykelet in hornblendite. [3] Dyke in Cpx hornblendite.
Abbreviations: (qtz) mzd: (quartz) monzodiorite, ton: bt + grt ± crd bearing tonalite, mzn: monzonite.
DI: differentiation index (CIPW normative *Q* + Ab + *Or* + Ne), Mg#: MgO/(MgO + FeO) molar, all Fe is as FeO, Eu/Eu*: $Eu_N/\sqrt{(Sm_N{*}Gd_N)}$. Normalization factors from Sun and McDonough (1989), CI chondrite.

maximum values in the pyroxene hornblendite of 479 ppm and 137 ppm in the gabbros.

The amphibole belongs to the hornblende group (Leake et al., 1997). Cumulus composition in the ultramafic rocks of UP is magnesiohastingsite, while the intercumulus composition corresponds to pargasite. In the monzodiorite hornblende composition is mainly magnesiohornblende and minor edenite. The Mg# in the amphibole decreases from 0.77 in hornblende pyroxenites to 0.65–0.58 in hornblendites. In the monzodiorite the Mg# varies from 0.70 to 0.62 in the Hbl and Plg rich layers, respectively (Table 2). The Al^{VI} (a.p.f.u. normalized to 23 oxygens) is 0.35 in the Hbl pyroxenite, 0.30 in the hornblendites and 0.17 in the monzodiorite.

The amphibole in the ultramafic-mafic rocks of the Moat pluton is magnesiohastingsite. The Mg# varies from 0.74 in hornblendes of the Px hornblendite and 0.64–0.63 in the gabbros. The Al^{VI} also decreases from 0.33 in the Px hornblendite to 0.27–0.21 in the gabbros.

The Cr content of amphiboles in the ultramafic-mafic rocks of UP and Moat pluton is less than 500 ppm, with a single value of ~550 ppm in a hornblendite of UP.

Al^{VI} is pressure dependent (Larocque and Canil, 2010), and it was determined experimentally that amphiboles crystallizing before plagioclase (i.e. at pressure greater than 4 kbar, Grove et al., 2003) have Mg# and Al^{VI} content greater than 0.70 and 0.3, respectively (e.g. Pichavant and Macdonald, 2007; Andújar et al., 2015).

Opaque minerals are mainly oxides. They appear as polycrystalline cumular aggregates 1–5 cm long in Hbl pyroxenites of UP. Their

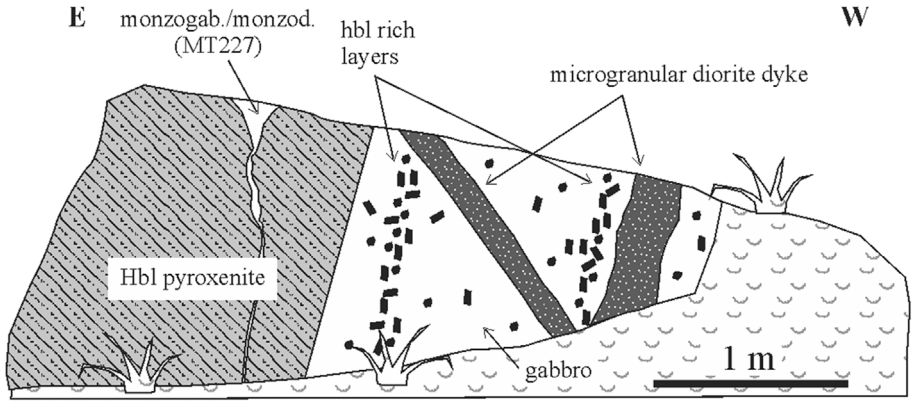

Fig. 5. Schematic drawing of a natural exposure in the hornblende pyroxenite core, showing layering of hornblende pyroxenite and gabbro. The Hbl pyroxenite bears subvertical monzogabbro/monzodiorite segregations, and the gabbro layer has parallel hornblende rich layers with oriented hornblende crystals (black dots). Microgranular diorite dykes cross-cut the sequence. *(single column fitting)*.

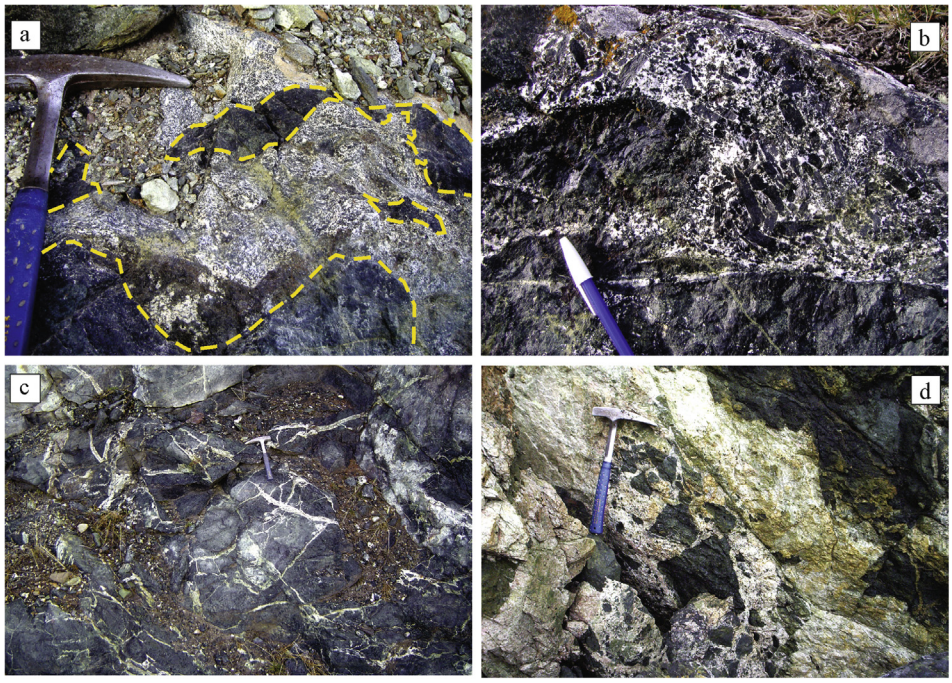

Fig. 6. Field relations and textures in the ultramafic-mafic section. (a) Mingling between medium-grained hornblendite (black, outlined) and gabbro (see location in Fig. 3b). (b) Anastomosing pegmatitic gabbro segregation (sample MT139) in hornblende pyroxenite, with large euhedral hornblende crystals oriented parallel to walls (hornblende crystals in the dyke are larger and more euhedral than in the Hbl pyroxenite host, and pyroxene is absent (top of pen for scale)). (c) Anastomosed, late stage monzonite dykelets in hornblendite (hammer for scale, location in Fig. 3b). (d) Brecciated hornblendite filled in by monzonite (hammer for scale). *(2 column fitting)*.

concentration and grain size decrease towards more differentiated rocks, where they occur as intercumulus phases. The most abundant oxide is magnetite with low Cr_2O_3 content (0.38–0.10% in Hbl pyroxenites and hornblendites, respectively). Ilmenite is present both as discrete crystals intergrown with magnetite and as exsolution lamellae in magnetite. In Hbl pyroxenites, the ilmenite has high MgO content (11.8–7.7%). This oxide decreases in hornblendite ilmenites (MgO < 0.15%), along with less MgO concentration in the host magnetite. The oxide nodules in Hbl pyroxenites also bear ferro-spinel ($(Fe,Mg)(Fe,Al)_2O_4$), with 62–65% Al_2O_3, as discrete crystals intergrown with magnetite-ilmenite and as exsolution blebs in these two phases. The Cr_2O_3 content is also low in the ferro-spinel (0.8–0.4%, Al/(Al + Cr) > 0.99). Precipitation of Al-rich spinel is consistent of delayed plagioclase crystallization at high pressure or water content (e.g. Leuthold et al., 2015; see Section 6.3).

3.4. Whole rock geochemistry

Samples covering a rock spectrum from gabbros to monzonite dykelets, and the S-type tonalite were analyzed for major and trace element contents. Results are presented in Table 3 and the analytical procedure is given in the appendix (see location of samples in Figs. 2–3). Additional geochemical data, including those from hornblendites, is provided by Acevedo et al. (2002).

The UP shows a wide range in silica composition from ultrabasic to acid components. SiO_2 varies from 38.3% to 61.79% in the ultramafic-mafic section and from 53.69% to 64.0% in the intermediate section (Acevedo et al., 2002, this work). It is worth mentioning that even though late stage dykelets in ultramafic rocks (MTF2b and those in Acevedo et al., 2002) classify as syenite in the TAS diagram, their modal composition is monzodiorite, monzonite and quartz monzonite (Fig. 4, Table 1).

With the exception of the tonalite, the geochemical composition of both sections follow a mildly alkaline trend in a TAS diagram (Fig. 9a) and plot in the shoshonitic series field in a SiO_2 vs. K_2O graph (Fig. 9b), with K_2O/Na_2O > 0.5 in most samples (Table 3). Hornblendites, gabbros and diorites of the UP also have normative nepheline (CIPW 5-1% *Ne*).

While alkalis show a positive correlation with silica, the other major oxides decrease as silica increases, except for Al_2O_3 wt% (Fig. 9c–h). All samples define rather continuous linear trends in total alkalis, CaO, Fe_2O_3t, TiO_2 and P_2O_5 diagrams. Some scattering is seen for ultramafic rocks, especially in the SiO_2 – Al_2O_3 diagram (Fig. 9d), probably due to variably proportions of cumular phases and epidote (modal plagioclase is less than 0.1% in the analyzed samples). These data is in agreement with petrographic observations that indicate early and continuous

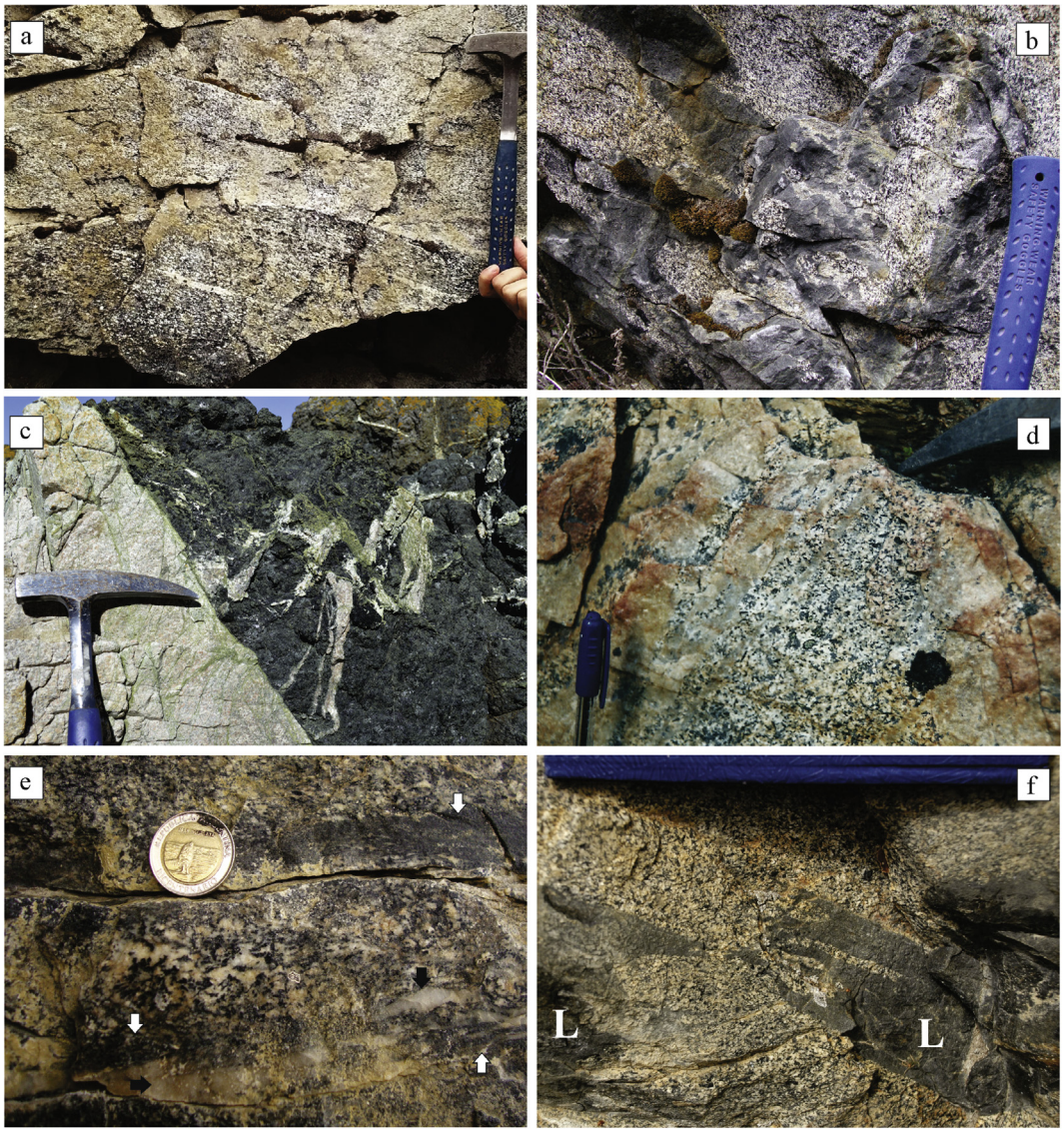

Fig. 7. Field relations and textures in the intermediate section (a-b, d-f). (a) Layering between gabbro/diorite and monzodiorite. Flow in the monzodiorite layer erosionated the underlying layer. (b) Disrupted and mingled fine-grained diorite/gabbro dyke (dark) in monzodiorite (handle of hammer for scale). (c) Monzodiorite dyke (related to the intermediate section, sample MT116) cross-cutting pyroxene hornblendite and its monzodiorite/monzogabbro seggregations (sample MT117) of the ultramafic-mafic section. (d) Differentiated segregation (leucocratic) in monzodiorite (cap of pen is 5 cm). (e) Diffuse enclaves of metapelite (white arrows) in monzodiorite close to the contact with country rock, and associated quartz rich veins (black arrows). (f) Lamprophyre dyke (L) back-veined with host monzodiorite (width of photo 22 cm). *(2 column fitting)*.

crystallization of pyroxene, amphibole, Fe—Ti oxides, apatite and sphene. Al_2O_3 shows a two-fold behavior (Fig. 9d). In the ultramafic-mafic section, even in non cumular gabbros/diorites (lacking cumular textures or Eu anomaly) there is an increase in Al_2O_3 up to ~50% SiO_2, then it shows a planar trend or slightly decreases up to monzonite dykelets. Delayed appearance of plagioclase may be responsible of this break at ~50% SiO_2.

The S-type tonalite plots in the calc-alkaline and peraluminous (A/CNK 1.23) fields in TAS (Fig. 9a) and A/CNK vs. A/NK (not shown) diagrams, respectively, that departs from the mildly alkaline and metaluminous trends of the UP.

Trace elements of rocks from both sections (Fig. 10a) show subduction-related composition in a spider diagram, with typical spiked pattern, Nb, Ta and Ti troughs, K and Sr spikes and enrichment of LILE relative to HFSE (Rb/Zr 0.35–1.73). The late stage dykelet of the ultramafic-mafic section, and to a lesser extent the monzodiorite dyke of the intermediate section, are the most enriched in incompatible elements (and SiO_2), especially Rb, Ba, Zr, Hf. The Ni and Cr contents in the UP are low (7–200 ppm Cr, 5–102 ppm Ni), with maximum values in the ultramafic facies.

Rare earth elements normalized to chondrite show enrichment of LREE relative to HREE (Fig. 10b), with $(La/Yb)_N$ ratios varying from 6 to 13.5 in the ultramafic-mafic section, and from 9 to 13.5 in the intermediate section (Table 3). The rocks display similar patterns in the diagram, except the dykes. The synmagmatic gabbro dyke shows a strong depletion in LREE, a trend that diminishes gradually towards the most evolved rocks. This is a behavior typical of this suite (González Guillot et al., 2009) and is due to the high content of hornblende (in agreement with their high contents of Fe_2O_3t and MgO), which incorporate preferentially MREE, and to a lesser extent HREE, relative to LREE (Rollinson, 1993). The late stage monzonite dykelet in the ultramafic-mafic section shows a strong negative Eu anomaly (Eu/Eu* 0.42, Fig. 10b, Table 3), which along with a negative peak in Sr (Fig. 10a), suggests it derives from a melt that experienced plagioclase fractionation. On the contrary, most gabbros/diorites show no Eu anomalies, either positive or negative, and the monzodiorites show a

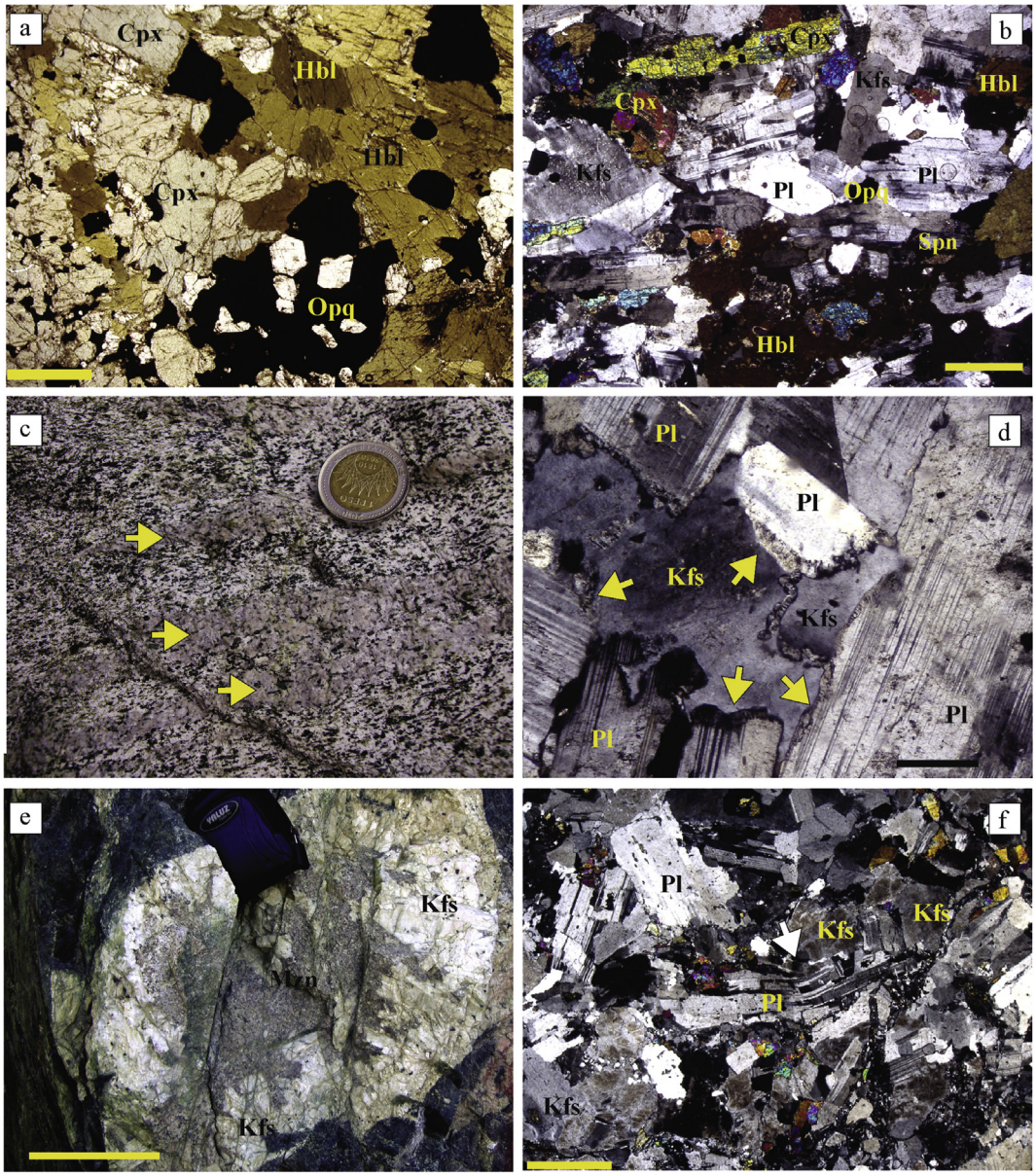

Fig. 8. Textures in ultramafic, mafic and intermediate rocks (a and e-f ultramafic-mafic section, b-d intermediate section). (a) Photomicrograph of cumular Hbl pyroxenite with diopside (Cpx), hornblende (Hbl) and opaque (Opq) + apatite nodules surrounded by anhedral (intercumulus) Hbl + Opq (parallel polars, bar 1 mm). (b) Photomicrograph of a monzodiorite with magmatic foliation: oriented crystals of plagioclase (Pl) and diopside (Cpx), and interstitial K-feldspar (Kfs), poikilitic hornblende (Hbl) and sphene (Spn; crossed polars, bar 1 mm). (c) Monzonitic lenses (arrows) in monzodiorite. (d) Photomicrograph of monzodiorite showing partial replacement of plagioclase by interstitial K-feldspar (arrows) developing myrmekite-like structures on plagioclase margins. No internal deformation of grains is visible (crossed polars, bar 250 μm). (e) Zonation in late stage monzonite dykelet showing a nucleus of monzonite (Mzn) surrounded by K-feldspar megacrysts (bar 5 cm). (f) Photomicrograph of a late stage monzonite dykelet in hornblendite with subgrain development and recrystallization, undulatory extinction and combed plagioclase crystals (white arrow). Hydrothermal brecciation and precipitation of epidote stresses deformation (crossed polars, bar 1 mm). *(2 column fitting)*.

slight negative anomaly (Eu/Eu* ~0.88, Table 3). Only one gabbro shows subtle geochemical evidence of crystal accumulation (MT3), with 21% Al_2O_3, distinctive positive peak in Sr in the normalized diagram (Fig. 10a) and a slight positive Eu anomaly (Eu/Eu* 1.09, Table 3).

The monzodiorite dyke of the intermediate section shows a trough-like REE pattern similar to that of the Ushuaia Peninsula Andesites (UPA), indicative of hornblende fractionation, although its major element composition (K_2O, Na_2O, TiO_2, CaO, Al_2O_3, Fig. 9, see also Fig. 12), Nb–Ta contents and modal composition preclude any genetic relationship to this suite.

4. Geochronology

We present three new LA-ICP-MS U–Pb zircon ages for the UP, and one for an andesitic dyke (P16) from the Ushuaia Peninsula Andesites (UPA) (Fig. 11, see location of samples in Figs. 1–2). Analytical techniques are provided in the appendix and in a supplementary file, along with a table (Table S2) with the analytical results. The UP samples correspond to a pegmatitic gabbro segregation within hornblende pyroxenite (MT139, ultramafic-mafic section) and two monzodiorites (MT112 and MT113, intermediate section). The UPA dyke represents one of the latest pulses of the suite.

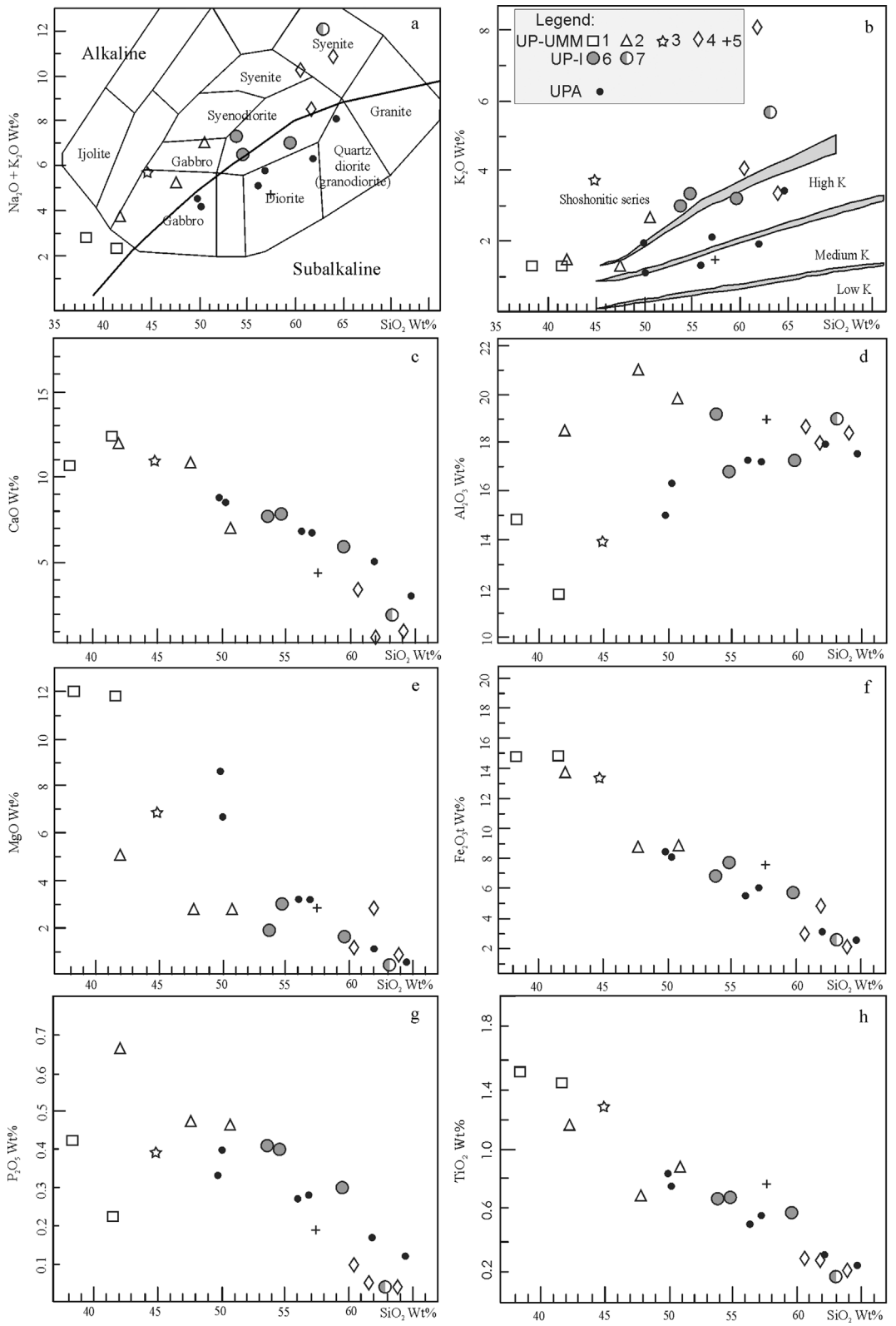

Fig. 9. Harker diagrams of UP (Acevedo et al., 2002 and this work) and Ushuaia Peninsula Andesites (dots) for comparison (González Guillot et al., 2011). Legend (1–5 ultramafic-mafic section, 6–7 intermediate section): 1 hornblendite, 2 gabbro, 3 synmagmatic gabbro dyke in hornblendite, 4 late stage monzonite dykelet, 5 bt + grt ± crd tonalite, 6 monzodiorite/qtz monzodiorite, 7 monzodiorite dyke cross-cutting the ultramafic-mafic section. Division lines in (a) and (b) are from Irvine and Baragar (1971) and Rickwood (1989), respectively. *(1.5 column fitting)*.

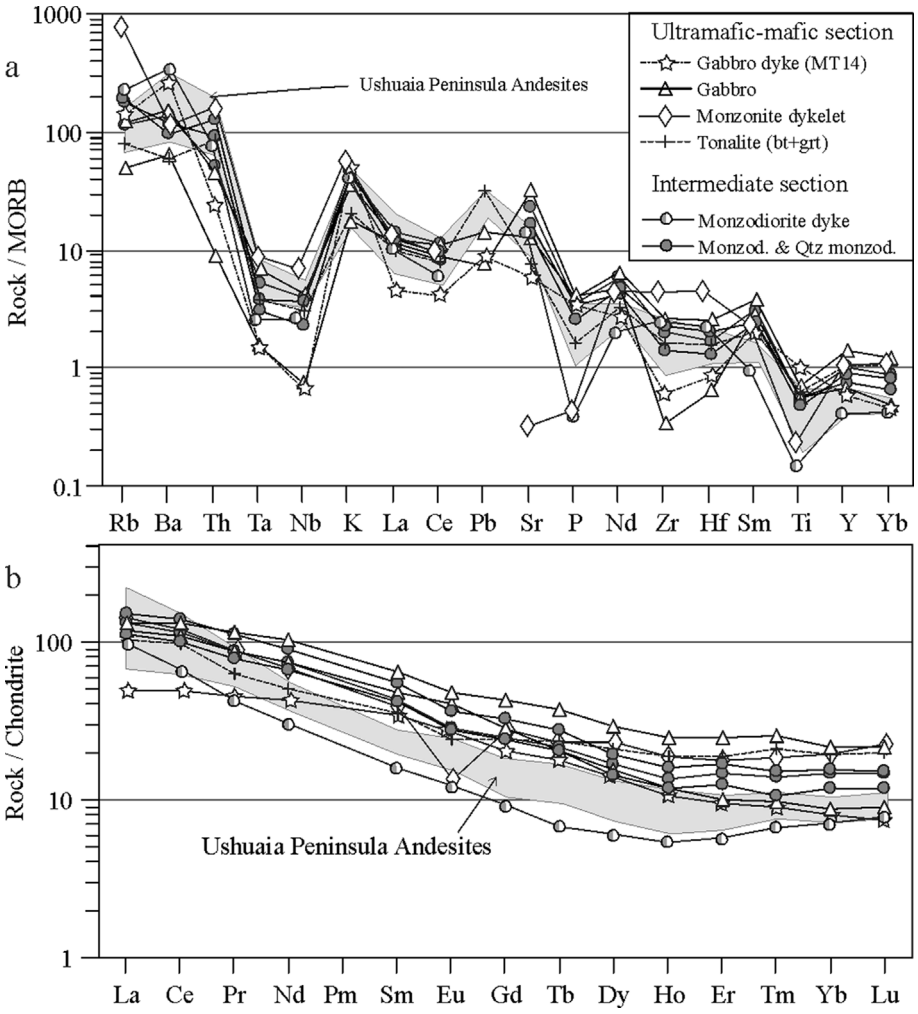

Fig. 10. (a) Trace element expanded diagram of UP, normalized to MORB (Sun and McDonough, 1989). (b) REE expanded diagram of UP, normalized to chondrite (Sun and McDonough, 1989). The field of the Ushuaia Peninsula Andesites is indicated for comparison (González Guillot et al., 2011). *(single column fitting)*.

4.1. Results

4.1.1. Sample MT139 (gabbro segregation in hbl pyroxenite)

Thirty seven zircon grains were analyzed on the pegmatitic gabbro (MT139). Large grain size is characteristic. The crystals vary from colourless to brownish yellow. The crystals analyzed in this study are characterized by an almost complete absence of crystal faces, and most of them are angular to subangular, presumably as a result of fracturing during mineral separation. A few of them are subrounded, characteristic of mafic rocks, and some likely owing to disequilibrium with the medium, causing incipient resorption during interaction with the magma.

The data show a span of ages from 80 to 64 Ma (Table S2, Fig. 11a–b). An average age 75.0 ± 1.0 (MSWD 14) was obtained leading us to interpret this as the crystallization age of the gabbro. Another population of 4 grains around 66 Ma is interpreted as Pb loss processes.

4.1.2. Sample MT112 (monzodiorite)

Twenty zircon grains from the monzodiorite were analyzed. All the zircons were relatively coarse-grained, perfectly euhedral, clear, colourless, stubby square prismatic grains with simple terminations, and showed no visible growth zoning or inherited cores. The data set reported by the laboratory shows a constant $^{206}Pb/^{238}U$ age between 73 and 75 Ma, with a weighted average at 74.0 ± 0.4 Ma (MSWD 0.56) (Fig. 11c–d). We interpret this as the age of emplacement and crystallization of the rock.

4.1.3. Sample MT113 (monzodiorite)

Nineteen zircon grains were analyzed from the monzodiorite. Two populations are present, a group with oblate short prismatic morphologies and a small group characterized by prismatic clear elongated crystals. Some of the oblate crystals show irregular zoning typical of zircons in mafic igneous rocks. The prismatic zircon grains mainly display regular growth zoning.

The data (Table S2, Fig. 11e–g) shows two main populations, one around 70.9 ± 1.7 Ma (MSWD 2.8) that we interpret as the age of emplacement and crystallization of the monzodiorite. Another population with a good fit on the concordia line is around 145.9 ± 2.1 Ma. Other single ages around 98 Ma and > 520 Ma are also registered. We interpret these last ages as wall rock contamination (see Section 6.3).

4.1.4. Sample P16 (andesitic dyke, UPA)

Forty-four zircon crystals were analyzed. The zircons are clear, and commonly have growth zoning. Different sizes are common and they have elongate to oblate, subhedral to euhedral prismatic morphologies; the elongate prismatic crystals are the most common.

The data shows an important quantity of inherited zircons up to Paleoproterozoic. Considering the data obtained (Table S2, Fig. 11h–k) a weighted average age of 84.1 ± 1.6 Ma (MSWD 8.4) is considered to be the best estimate of the age of emplacement and crystallization.

The results provided here for the UP are similar to that obtained by

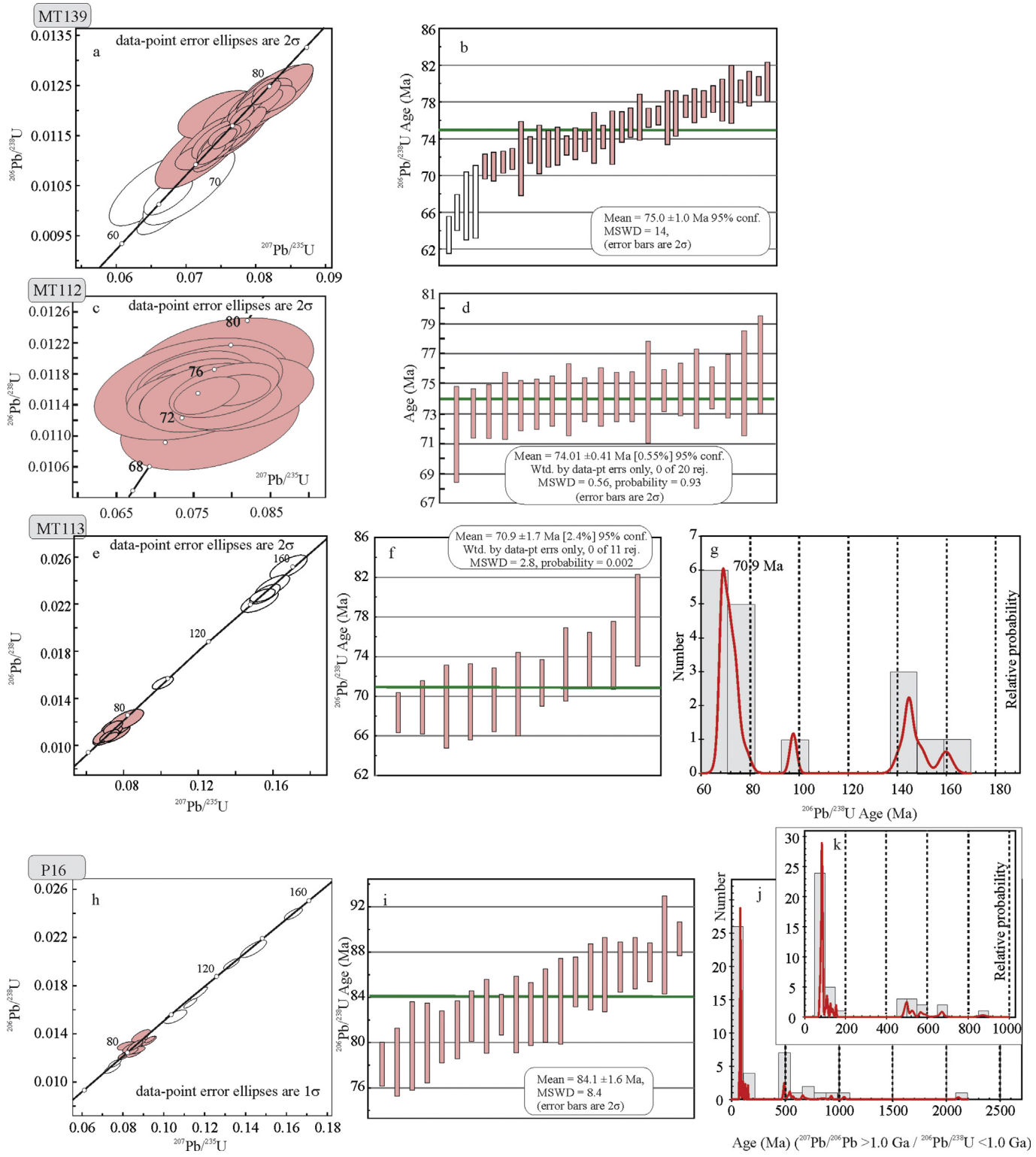

Fig. 11. U-Pb isotopic data on zircons from the UP (MT samples) and UPA (sample P16). (a, c, e, h) Wetherill concordia plots. (b, d, f, i) Calculated means with errors reported at the 2σ level. (g, j, k) Age versus probability diagrams. White ellipses (in a, e, h) and bars (in b) were not included in age calculation. MT139: pegmatitic gabbro segregation in Hbl pyroxenite, MT112-MT113: monzodiorite, P16: andesitic dyke (UPA). *(2 column fitting)*.

Barbeau et al. (2009) in a felsic dyke cross-cutting hornblendites (U—Pb zircon age of 75 ± 2 Ma –our sample MTF2). All the U—Pb results differ significantly from earlier K—Ar (whole rock and hornblende) ages in the range 113–102 Ma for the UP, and 77–104 Ma for the UPA (Ramos et al., 1986; Acevedo et al., 2002; Elsztein, 2004; Peroni et al., 2009). They also show the UPA suite is older than UP, contrarily to what depicted the previous K—Ar results.

5. Thermobarometry

Intensive variables, pressure (P) and temperature (T), were calculated for the crystallization of the UP using different approaches.

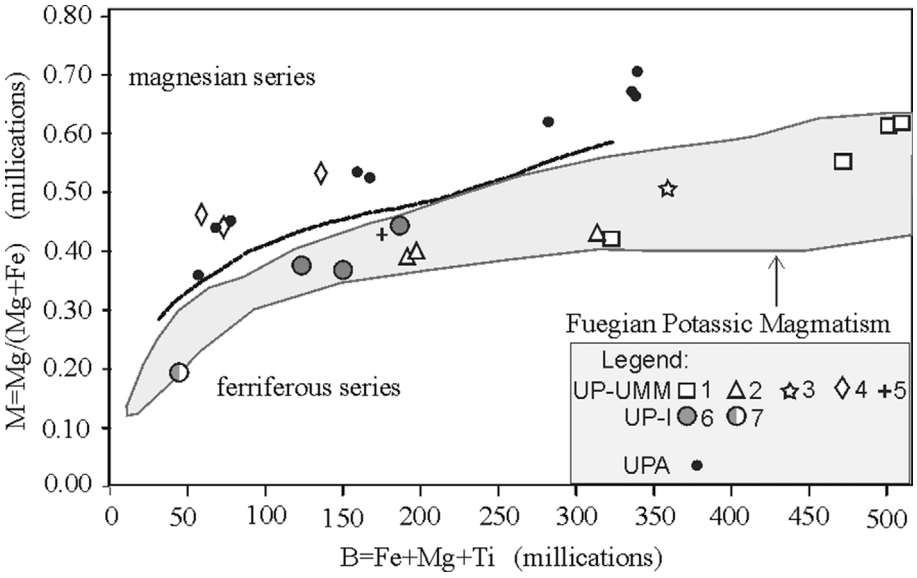

Fig. 12. B-M diagram of Debon and Le Fort (1988) with data from UP, the Ushuaia Peninsula Andesites (González Guillot et al., 2011) and other plutons of the Fuegian Potassic Magmatism (Moat pluton, González Guillot et al., 2009; Kranck and Jeu-Jepén plutons, González Guillot et al., 2012). Same references as in Fig. 9. *(single column fitting)*.

Calculation of T was necessary to employ some T-dependent geobarometers. Additionally, some geothermometers are P-dependent, thus iteration was done in such cases, whenever it yielded realistic results (see Supplementary file, Table S3). Additional data of hornblende barometry of Moat pluton is included.

5.1. Thermometry

Temperature for the Hbl pyroxenite (MT61) varies from 844 °C to 1025 °C (average 939 °C) using amphibole compositions and the thermometers (P independent) of Ernst and Liu (1998), Ridolfi et al. (2010a) and Ridolfi and Renzulli (2012). Core and rim compositions yielded similar results. When applying the pyroxene thermometer of Putirka (2008, modified after Nimis and Taylor, 2000), higher values of T are obtained, in the range from 1014 °C to 1063 °C (for 1.9 and 7.0 kbar, respectively –see below).

The monzodiorite (MT89) yielded temperatures of 753 °C to 859 °C, using the thermometers of Ernst and Liu (1998) and Ridolfi et al. (2010a) for amphibole composition (P independent), respectively. An average of 790 °C is obtained considering also the plagioclase-hornblende thermometer of Holland and Blundy (1994) (at 3.0 kbar). Amphibole composition is not suitable for applying the thermobarometer of Ridolfi and Renzulli (2012), and iteration between equations (32a) and (32d) of Putirka (2008) yielded no realistic results.

5.2. Barometry and contact metamorphism

Pressures in the Hbl pyroxenite (MT61) range from 9.36 kbar to 5.09 kbar (average 7.10 kbar), according to the amphibole barometers (T independent) of Ernst and Liu (1998), Ridolfi et al. (2010a), Ridolfi and Renzulli (2012) and Krawczynski et al. (2012) (modified from Larocque and Canil, 2010). As with temperature, core and rim results overlap. Estimates based on pyroxene compositions yield much lower results, ~1.93 kbar for 1014 °C (equations of Nimis (1999) (MA barometer) and Putirka, 2008 (eq. (32a), modified after Nimis, 1995)). Average pressures for the hornblendes in the hornblendites (data from Acevedo, 1996) range from 6.99 kbar to 4.80 kbar (using the above amphibole barometers).

For comparison we applied the same barometers than above to hornblendes from the ultramafic and mafic rocks of the Moat pluton (González Guillot et al., 2009) referred to in Section 3.3. Average pressures yielded 7 kbar for the pyroxene hornblendite and 4.4 kbar for the gabbro dyke and segregations.

Pressures for hornblende crystallization in the monzodiorite of UP range from 4.60 to 1.92 kbar (average 3.20 kbar) using the hornblende barometers of Ernst and Liu (1998), Ridolfi et al. (2010a), Schmidt (1992), Krawczynski et al. (2012), and the T-dependent formulation of Anderson and Smith (1995) (at 790 °C). No differences were observed between hornblende core and rim results. The pyroxene barometers of Nimis (1999) and Putirka (2008) gave no realistic results. Recently, a barometer based on normative composition was developed for silica rich granitoids (Yang, 2017). The monzonite dykelet (MTF2-b) is the only sample suitable for the calculation and gives a result of 2.47 kbar.

In the Jeu-Jepén pluton (same suite as UP, González Guillot et al., 2012) Ridolfi et al. (2010b) found magnesiohastingsite megacrysts, hosted in monzonite, with corona reactions. The megacrysts yielded pressures of crystallization of 12–25 kbar (959–1029 °C), while the host monzonite crystallized at shallow conditions (Ridolfi et al., 2010b).

On the other hand, the contact metamorphic aureole around the UP, developed on low grade metapelites (prehnite-pumpellyite facies, Caminos, 1980), provides further information related to the depth of emplacement of the pluton. An inner envelope, 10–15 m wide (Fig. 2), shows strong recrystallization, with coarsening of grain size (up to ~500 μm), and granoblastic polygonal textures. The foliation of the country rock has been erased in this region. The mineral assemblage in this zone is quartz + biotite + garnet + plagioclase + andalusite + cordierite ± fibrolite ± muscovite. Metasedimentary enclaves in the tonalite in contact with the country rock bear porphyroblasts of garnet + biotite + amphibole, and other show restitic assemblages with orthopyroxene and spinel. The inner zone is surrounded by a wider envelope with lesser degree of both recrystallization and suppression of sedimentary or tectonic fabrics. The paragenesis includes biotite + garnet + plagioclase + quartz + K-feldspar and occasional andalusite. This zone extends up to 600 m to the east and at least 500 m to the north of the pluton. The outer zone (up to 3 km to the east from the contact) is characterized by the appearance of only biotite flakes.

The paragenesis provided above correspond to associations of the facies series 1c or 2a of Pattison and Tracy (1991), which indicate a pressure range of 1.5–3.0 kbar or 2.5–4.0 kbar, depending on the P-T location of the sillimanite-andalusite reaction curve. The aluminosilicate may have appeared through the reaction Ms + Chl + Qz = Als + Bt + Crd + V (equation (4) of Pattison, 2001), which indicates a pressure no higher than 4 kbar. The facies series indicated above are equivalent to the bathozones P1 and lower P2a of Pattison (2001), thus constraining pressure to a maximum of about 3.5 kbar. Garnet may appear as an “extra” phase in this rocks

favoured by the presence of MnO and CaO in the slates, and not as a product from the breakdown of staurolite + muscovite + quartz in pelites at higher pressures (Pattison and Tracy, 1991; and references therein). The presence of garnet-bearing and garnet-absent laminae in a same thin section, or the almost absence of this mineral in the metapelites within the aureole around the Moat pluton (considered of similar grade; González Guillot et al., 2009), favours this interpretation.

Therefore, we interpret pluton emplacement and contact-metamorphism pressures have been in the range ~2.5–3.5 kbar.

6. Discussion

6.1. Distinguishing between the UP and the Ushuaia Peninsula Andesites (UPA)

It is worth taking into consideration the relationship between the UP and the andesitic dykes at the neighbouring Ushuaia peninsula (UPA), necessary for the following discussions, and in order to avoid further misleading interpretations, many of which were based on the previous erroneous K−Ar ages. The petrography and chemistry of the UPA were given in detail elsewhere (González Guillot et al., 2011), here we make a comparison of both suites.

The UPA suite has been genetically correlated with the UP in previous works (Acevedo et al., 2002; Peroni et al., 2009), the “roof facies” of Peroni et al. (2009). However, the petrography, geochemistry and age strongly suggest these units represent two different magmatic events, evolved from different parental magmas, and separated in time.

Concerning mineralogy, the main lithologies of UP contains no to small amounts of quartz (Table 1), following a monzonitic to alkaline -silica saturated-trend (Lameyre, 1987). On the contrary, the Ushuaia Peninsula Andesites evolve to quartz rich rocks, following a calc-alkaline –granodioritic- trend (Lameyre, 1987) (Fig. 4).

Chemically, the UP shows a mildly alkaline trend whereas the UPA is calc-alkaline (Fig. 9a). The K_2O content is also different, much higher in the UP (Fig. 9b). Integrating the major oxides in a B-M diagram (Debon and Le Fort, 1988), two different series are again evident. While UP plots in the ferriferous series field, as do the other plutons of the Fuegian Potassic Magmatism, the Ushuaia Peninsula Andesites plot in the magnesian field (Fig. 12). The late stage monzonite dykelets in the ultramafic-mafic section of UP plot in the magnesian field as well, and merge with the UPA samples, although other chemical parameters (e.g. alkalies, CaO, P_2O_5 and REE, Figs. 9–10) are quite different. Additionally, the REE pattern of the UP shows significant differences with the Ushuaia Peninsula Andesites (Fig. 10b). The UPA is marked by a strong upward concave pattern and a lower HREE content; the last features were attributed to significant hornblende fractionation combined with a slab or subducted sediment melt component in the source (González Guillot et al., 2011).

Finally, our new U−Pb zircon ages show the youngest dykes of UPA are at least ~6 m.y. older than the oldest UP rocks (ultramafic-mafic section).

It is worth mentioning that the tonalites, considered to be UP magmas contaminated with country rock (Section 6.4), differ from UPA, but are similar to UP, in plotting in the ferriferous series (Fig. 12) and in containing higher values of HREE (Fig. 11). This, together with their peraluminous chemistry and mineralogy akin to S-type granites, suggest that UPA did not derive from UP-type magmas by crustal contamination.

Therefore, the mineralogy, geochemistry and age presented here (and in González Guillot et al., 2011) demonstrate the UP and UPA belong to independent suites.

6.2. Mode of emplacement and pluton growth

Recent concepts on pluton growth, reinforced by high precision U−Pb geochronology, conceive an incremental construction by in-situ amalgamation of small volumes of magma (e.g. McNulty et al., 2000; Petford et al., 2000; Vigneresse and Clemens, 2000; Glazner et al., 2004; Bartley et al., 2008; de Saint-Blanquat et al., 2011; Annen, 2011; Miller et al., 2011), in contraposition to the old paradigm of ballooning (e.g. Pitcher, 1979; Paterson et al., 1989, 1991). This process may take a short (~0.1–0.5 m.y.; e.g. Michel et al., 2008; Leuthold et al., 2012; Bucholz et al., 2017) or a significant time span (~3–10 m.y.; e.g. Coleman et al., 2004; Matzel et al., 2006), mainly with direct relation to pluton size (de Saint Blanquat et al., 2011). By this mechanism, successive magma batches intrude already, or partially, consolidated ones. The regional stress field exerts significant control on magma ascent, emplacement and pluton shape (Brown and Solar, 1998; Vigneresse and Clemens, 2000).

Contact relationships (Section 3) in the UP and the U−Pb zircon ages indicate the pluton grew by amalgamation of two main batches of magma that gave place to the ultramafic-mafic section on the one hand (~75 Ma), and to the intermediate section on the other hand (~74-71 Ma). The second series appears to have under-accreted the first one. Nevertheless, (i) the different generations of dykes, as those of gabbro/diorite into gabbro/diorite (Fig. 3b) or lamprophyres, (ii) autoliths, and (iii) mingling between hornblendite-gabbro (Fig. 6a) and gabbro-gabbro, suggest these two main pulses were built up by successive smaller injections of magma. Moreover, the deformed gabbro/diorite autoliths in monzodiorites, the interlayering between these lithologies, the evidences of magmatic erosion (Fig. 7a), and the lack of a sharp contact, suggest simultaneous injection of some pulses of mafic and intermediate magmas. It is worth to remind that the monzodiorites of the intermediate section bear angular enclaves of ultramafic rocks and their pegmatitic gabbro segregations of the ultramafic-mafic section, indicating a time interval long enough to allow the crystallization of the latter before the emplacement of the monzodiorites, even though some radiometric ages overlap when the uncertainties are considered.

In plutons grown by slow accretion of sills or dykes, each successive intrusion solidifies before the injection of the next one (Annen, 2011). Therefore, magma accretion rate in the UP should have been high enough to allow incomplete consolidation of the previous batches. Considering the relationship of pluton size and rates of construction (Annen, 2011; de Saint Blanquat et al., 2011; Blundy and Annen, 2016), the UP should have been built up closer to, or even in a shorter time than our minimum estimate of 1.4 m.y. based in the conventional (LA-ICP-MS) U−Pb ages presented in Section 4 (compare for example the faster construction rates detected by ID-TIMS in the larger Torres del Paine pluton, Michel et al., 2008; Leuthold et al., 2012). Therefore, these ages may not adequately picture the time elapsed in its construction. Additionally, the UP is small (even considering its extension in subsurface) and a fast cooling rate is expectable (de Saint Blanquat et al., 2011; Blundy and Annen, 2016). However, (i) the preservation of fabrics indicative of magma chamber processes (see next section), (ii) evidences of country rock partial melting and (iii) its plastic deformation close to the pluton margins (described below) are indicative of low cooling rates and a high thermal environment during intrusion.

The foliation in the country rock adjacent to the pluton is steeply dipping and tends to be parallel to the margins. Along the western contact, the foliation dips outward, whereas along the northeastern and eastern contacts, the foliation dips inward (Fig. 13). Folding of the foliation also occurs close to the eastern and western margins. On the other hand, the UP has an internal fabric parallel to the pluton margins close to the country rock (Fig. 13), well developed in gabbros, diorites and monzodiorites. This fabric consists of crystal orientation, which defines a steeply dipping magmatic foliation. When present, layering, schlieren, elongated autoliths and metasedimentary enclaves tend to be parallel to this foliation. Thus, the foliation both in the pluton and country rock is parallel to regional structures only along the NE margin, precisely where the contact is parallel to those structures; while oblique to perpendicular on the NW and SE margins. This suggests the country rock was plastically deformed during amalgamation of the pluton.

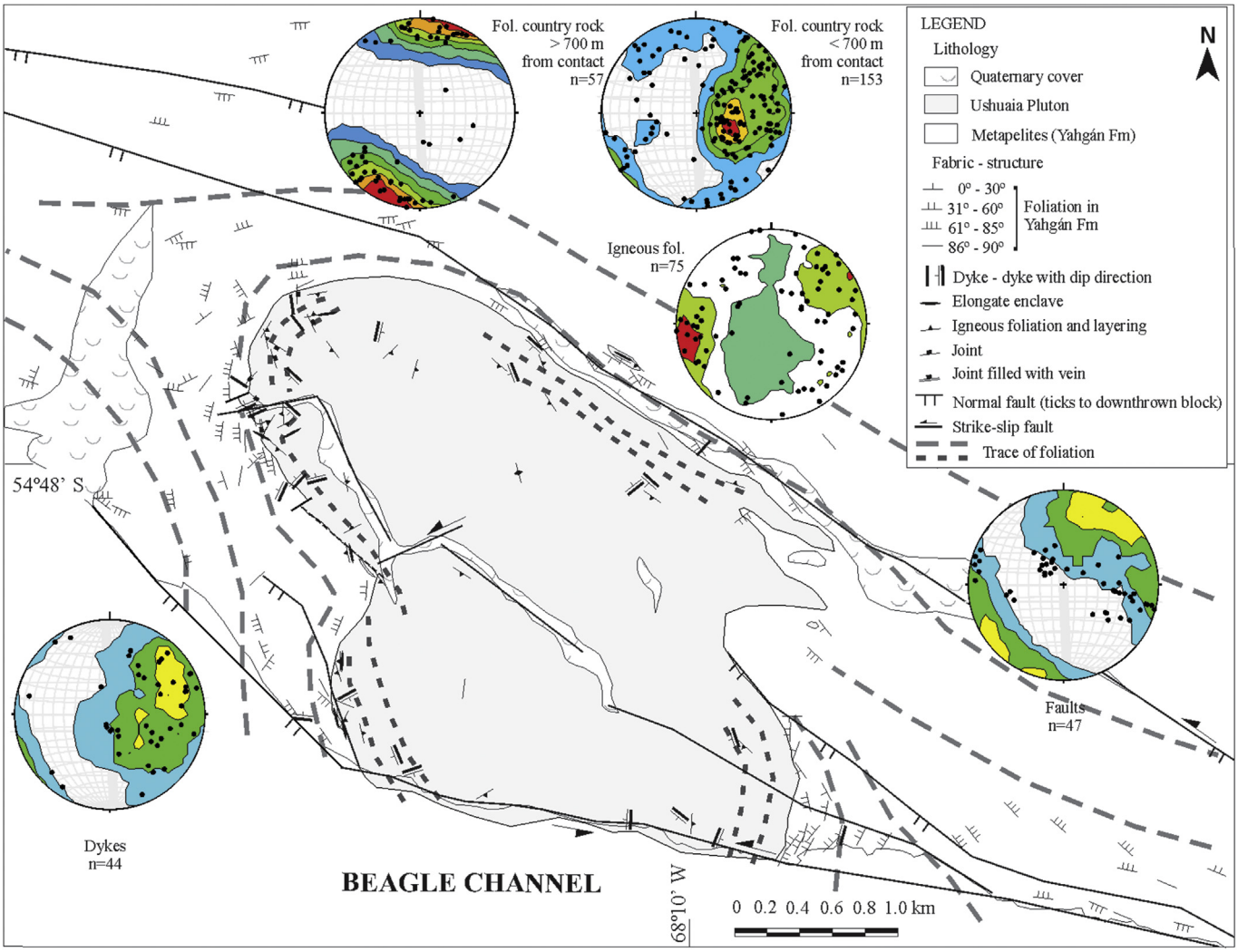

Fig. 13. Structural features in the UP and in the surrounding country rock. Stereonets are equal area, lower hemisphere, poles to planes. The data was acquired all around and inside the pluton. Number (n) of measurements indicated for each plot. Kamb contours for poles every 2 sigma. For strike-slip and oblique-slip faults slikenlines are indicated along with kamb contours for poles to planes (Stereonet software by Allmendinger et al., 2013; Cardozo and Allmendinger, 2013). *(1.5 column fitting)*.

Additionally, the parallelism between foliation and pluton margins or layering is typical of primary igneous features (Paterson et al., 1989, 1998; Vernon, 2000), caused by magmatic flow during injection (Barbey, 2009), deformation by subsequent magma intrusion (John and Blundy, 1993), or compaction during melt extraction (Fiedrich et al., 2017), independent of regional tectonic stress (Barbey, 2009; de Saint Blanquat et al., 2011).

Subsolidus fabric, i.e. deformation in the absence of melt, is absent or negligible in the foliated rocks, ruling out a tectonic origin for the foliation. Therefore, foliation is interpreted as igneous, caused by flow in the presence of melt without interference among crystals during rotation (Paterson et al., 1998; Vernon, 2000). Solid-state deformation features were only seen in the late stage monzodiorite-monzonite-granite dykelets of the ultramafic-mafic and intermediate sections (Section 3.2, Fig. 8f), which are typical of deformation in a brittle-ductile regime (Hibbard, 1995). We interpret them as submagmatic fabrics, developed during compaction and extraction of low proportions of melt, allowing interference and plastic deformation of crystals ("submagmatic flow" of Paterson et al., 1989), without significant development of foliation (c.f. Fiedrich et al., 2017). High vapour pressure may have facilitated deformation and/or stress associated to different injections.

On the other hand, the straight NE margin of the UP is parallel to regional structures, and in fact coincident with a fault that extends further beyond the pluton limits (Fig. 13). This suggests that emplacement was controlled by structural anisotropies in the country rock (e.g. McNulty et al., 2000; Petford et al., 2000).

Additionally, there occur numerous elongate metapelite enclaves around the pluton margins. Their elongation and internal foliation are parallel to the margins (thus parallel to the foliation of the country rock) and to the igneous foliation all along the pluton (Fig. 13); therefore, we interpret them not as stoping but isolation of wall rock during successive magma injection and lateral pluton growth.

6.3. Polybaric evolution of UP

The evidences of piecemeal construction of plutons arisen in the last years bring the magma chamber and in-situ magmatic differentiation concepts in conflict (Coleman et al., 2004; Glazner et al., 2004; Annen, 2011; Blundy and Annen, 2016). However, even though the small size of the UP and its piecemeal construction, evidences in favour of small-scale in-situ magma chamber processes (diversification) occur, and suggest at least transitory reservoirs with mobile magma. These are more evident in the ultramafic-mafic section.

Considering the Moat pluton has evolved in a similar way than UP (González Guillot et al., 2009), we combine the barometry results of

both. The high pressures of crystallization obtained from the hornblende compositions in hornblende pyroxenites and hornblendites (~7 kbar, Section 5.2) imply emplacement at shallow crustal levels (~2.5–3.5 kbar) of magma mushes loaded with pyroxene and hornblende crystals (± apatite, opaques) crystallized deeper in the system; the crystals being arrested at the place of entrainment, while the residual liquid flowed to the surroundings. Experimental results on hydrous magmas showed that hornblende precedes plagioclase crystallization at pressures above 4 kbar (Müntener et al., 2001; Grove et al., 2003; Ulmer, 2007; Nandedkar et al., 2014), thus in agreement with our hornblende barometry results. However, we detected no disequilibrium textures in hornblende crystals, i.e. resorption of margins or anhedral cores, under polarized microscope or the electron probe microanalyzer, as would be expected for hornblende transported from deeper sources. On the contrary, plagioclase crystallized prior to hornblende in the gabbro and monzogabbro segregations hosted in the ultramafic rocks, consistent with the hornblende barometry results of ~4 kbar. Therefore, these segregations occurred and crystallized at the site of emplacement. The pressures obtained by pyroxene barometry are too low, even lower than the pressure estimates from contact metamorphism. Although we consider no core to rim chemical reequilibration (Section 3.3), we dismiss this low pressure results.

The above interpretation is also supported by the Mg# and Al^{VI} contents in amphiboles, higher than 0.7 and 0.3, respectively, in the hornblende pyroxenites, and lower than these values in the gabbro segregations and dyke (Section 3.3); which reflects hornblende crystallization prior to and after plagioclase saturation, respectively (Klaver et al., 2017).

Emplacement of magma mushes in upper crustal reservoirs has been invoked elsewhere (e.g. Leuthold et al., 2014), and segregation of magma from the static crystal mush showed to be a common process (Mahood and Cornejo, 1992; John and Stünitz, 1997; Bachmann and Bergantz, 2004; Weinberg, 2006; Vernon and Paterson, 2008). The subvertical layering and foliation in the Hbl pyroxenite core (e.g. Fig. 5) is interpreted as a record of injection structures.

The very low contents of Cr and Ni in whole rock and minerals (Sections 3.3 and 3.4), along with the lack of olivine and Cr-spinel in the UP, suggest the magma from which the ultramafic rocks formed had already an evolved composition. Many examples of arc roots (Ulmer, 2007; Dessimoz et al., 2012) or moderate to high pressure experimental petrology (e.g. Müntener et al., 2001, Grove et al., 2003; Batanova et al., 2005; Ulmer, 2007; Nandedkar et al., 2014) showed that fractional crystallization of hydrous picrobasalt above ~1070 °C yielded dunite, wehrlite and Ol-pyroxenite cumulates and that hornblende pyroxenites, hornblendites and Hbl-gabbros crystallized from evolved liquids of basaltic andesite to andesite composition at lower temperature. Therefore, such a composition is assumed to have been the parental magma for the ultramafic rocks exposed in the UP. Fractional crystallization experiments of Nandedkar et al. (2014) found that hydrated andesitic magmas at 7 kbar only crystallize 50% in the window 1010-730 °C, the temperature range estimated for UP, thus being able to move as crystal mushes. At pressures of 7–8 kbar, from hydrated basaltic andesite or andesite, hornblende crystallizes close to the liquidus and has high Mg# (~0.80; Grove et al., 2003), similar to the hornblende composition in the hornblende pyroxenite of UP (Mg# 0.78, Table 2).

Other small-scale, in-situ magma processes can be cited in the ultramafic-mafic section. Some of the gabbro segregations contain irregular K-feldspar rich layers towards the contact with the ultramafic host, resulting in monzogabbro to monzonitic compositions indicative of further magma segregation. Several examples of mm-scale net veining of leucocratic material (rich in K-feldspar) occur, with evidences of above-solidus plastic motion, and coalescence of this material into cm-sized pods (Fig. 14). In Fig. 14, the host rock is a hornblende pyroxenite, and the pod and veinlets range from hornblende monzodiorite to pure K-feldspar. This phase concentrates in the pod and in thin selvedges against the hornblende pyroxenite, and escapes upwards as thin veinlets, showing local-scale differentiation. We infer the leucocratic material represents final droplets of melt that coalesced and migrated to form the widespread monzonite dykelets elsewhere in the ultramafic-mafic section. Therefore, the gabbro/monzogabbro segregations also evolved by in-situ differentiation. The strong negative Eu anomaly of the monzonite dykelet analyzed (Fig. 10b), which suggests plagioclase fractionation, holds this interpretation. Note also in Fig. 14 the hornblende concentration at the base of the pod, or the thin selvedges rich in hornblende bordering host inclusions that results in orbicular texture. Both represent in-situ hornblende crystallization and concentration of the more evolved liquid in the centre and top of the pod. This is like the melanosome selvedges around segregated liquids in granitoids presented by Weinberg (2006). Even in segregations of monzogabbro as thin as 2 cm, evidences of in-situ differentiation occur giving place to a selvedge of gabbro and a central zone of monzonite/syenite (e.g. the segregation pipe of Fig. 5).

6.4. Origin of the peraluminous border facies

Peraluminous granites have been traditionally considered as derived from crustal partial melts (Chappell and White, 1974), although later experimental work have shown they can derive from I-type hydrous magmas by significant crystal fractionation of amphibole above 6 kbar, without a crustal component (Müntener et al., 2001; Ulmer, 2007; Dessimoz et al., 2012; Nandedkar et al., 2014).

While hornblende fractionation in the absence of plagioclase was important in the evolution of the ultramafic-mafic section of the UP, several evidences point to an origin of the peraluminous tonalite by crustal assimilation at the site of emplacement and not by extensive fractionation alone.

The tonalite is minor volumetrically compared to the rest of the pluton, and occurs only as border facies between gabbro/diorite and country metapelites. It contains abundant surmicaceous enclaves with diffuse contacts, some of them with restitic paragenesis with orthopyroxene and spinel (Section 3).

In a A/CNK vs. A/NK plot (not shown), the rocks of UP and also the other plutons of the suite (Moat, González Guillot et al., 2009; Jeu-Jepén and Kranck, González Guillot et al., 2012), show an evolutionary trend towards the peraluminous field, and the only rocks that straddle the metaluminous-peraluminous divide are the late stage monzonite/syenite dykelets (with I-type paragenesis), but at ~1 of A/NK. The tonalite of the UP plots in the peraluminous field far from the divide and at an A/NK value of ~2.7. Additionally, the REE pattern of the tonalite (Fig. 10b) does not suggest significant hornblende fractionation (i.e. it does not have a trough-shape).

The above features suggest the tonalite represents a hybrid rock of mixed gabbro/diorite and anatectic melt derived from the surrounding metapelites (González Guillot and Acevedo, 2009). Water fluxed from the underlying gabbro/diorite parental magmas may have facilitated partial melting. In the intermediate section in contrast, the monzodiorites in contact with country rock only suffered minor assimilation and evolved to quartz monzodiorites (with I-type paragenesis) (Fig. 7e). Assimilation in monzodiorites is also evidenced by the populations of inherited zircons around 146 Ma (Section 4), similar to detrital zircons in the Yahgan Fm with ages in the range 105–158 Ma (Barbeau et al., 2009; Klepeis et al., 2010).

6.5. Timing of emplacement relative to regional tectonics

The new U—Pb ages indicate the UP crystallized during the Campanian-Maastrichtian (75-70 Ma, Barbeau et al., 2009; this work). The initiation of Andean orogeny and peak metamorphism is placed broadly at the beginning of the Late Cretaceous (Fildani et al., 2003; McAtamney et al., 2011; Calderón et al., 2012, 2016), more precisely prior to 86 Ma in Tierra del Fuego (Klepeis et al., 2010). However,

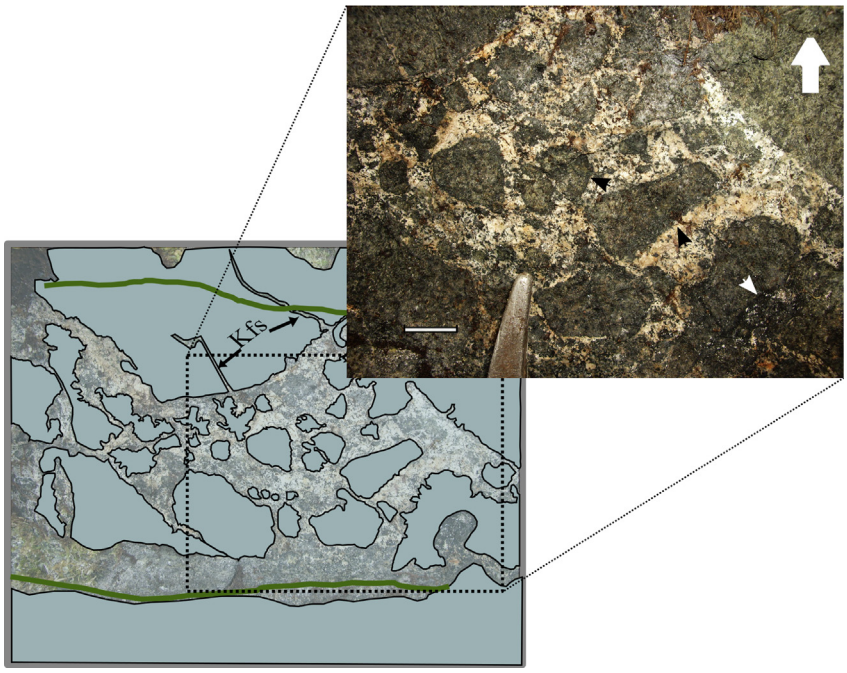

Fig. 14. Differentiated (monzodioritic) pod in hornblende pyroxenite, large white arrow points upwards. The pod is more mafic at the base and from the upper margin K-feldspar (Kfs) rich veinlets emanate upwards. The small white arrow on bottom right corner shows squeezed monzodiorite between pyroxenite fragments at the base of pod. Note rims of hornblende around it and around pyroxenite fragments within the pod (black arrows). Late stage epidote veinlets (green thick lines) cross-cut the pod. Bar is 2 cm. *(1.5 column fitting)*. (For interpretation of the references to colour in this figure legend, the reader is referred to the Web version of this article.)

Maloney et al. (2011) indicated that regional metamorphism at Cordillera Darwin was still taking place at ca. 73 Ma (U/Pb dating in monazite), i.e. coeval to the emplacement of the UP. Nevertheless, the UP and its aureole lack evidence of being overimposed by regional metamorphism.

The aureole around the UP provides further information supporting emplacement following the initial orogenic phase. The aureole in its inner zone, i.e. very close to the pluton, shows no foliation and experienced significant recrystallization with development of granoblastic and polygonal textures, indicating that mineral growth or textural recovery continued after deformation, regardless of its origin (i.e. regional or pluton-induced). Away from this inner zone, a margin-parallel foliation is progressively more developed defined by aligned biotite crystals, and garnet porphyroblasts are euhedral with matrix inclusions with schistosity (Si) continuous with the external schistosity (Se), without evidences of grain rotation (Fig. 15). This supports the aureole formed and the pluton emplaced post-kinematically. Some deflection of matrix folia around garnet porphyroblasts there exists, however. This not necessarily implies syn- or pre-tectonic growth, since it may be explained by deformation associated to magma emplacement or volume changes in the aureole in response to thermal expansion or metamorphic reactions (Paterson et al., 1991).

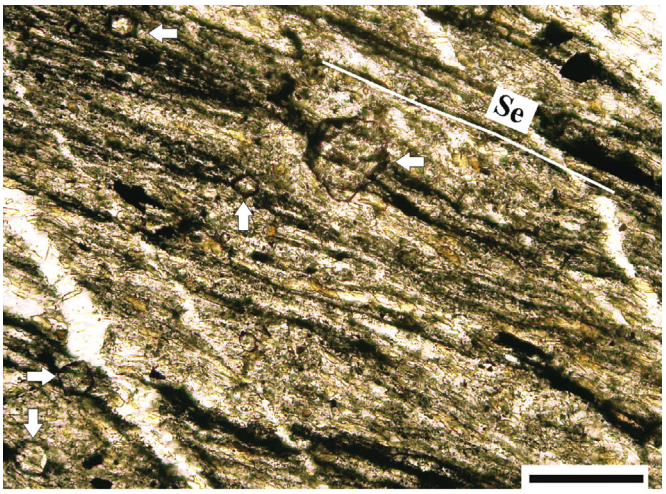

Fig. 15. Photomicrograph of a contact-metamorphosed slate from the aureole around UP. Euhedral garnets (white arrows) with matrix inclusions parallel to external schistosity (Se). No deflection of matrix is seen in this sample (parallel polars, bar 100 μm). *(single column fitting)*.

Notwithstanding, the UP emplaced during a recorded period of thrusting that propagated shortening towards the foreland until the Paleogene (Klepeis et al., 2010; Maloney et al., 2011; Torres Carbonell and Dimieri, 2013). This is consistent with a model of slab flattening responsible of a shift in the volcanic front away from the trench and the rear-arc shoshonitic magmatism (Stern et al., 1991; González Guillot et al., 2011), which provides the conditions for a locked (i.e. high degree of coupling) subduction system. On the other hand, the subvertical structures related to injection processes (gabbro dykes and monzodiorite pipe segregations in Figs. 3 and 5) suggest the pluton was not or only slightly tilted during subsequent thrusting.

Contrarily, Peroni et al. (2009) proposed the UP emplaced coeval with a dominant extensional component, based on meso and microstructures. They related this tectonic setting to stress partitioning due to oblique convergence subsequent to the closure of the Rocas Verdes marginal basin (Cunningham, 1993). The meso and microstructures described by Peroni et al. (2009) are equivocal and do not reflect our field and petrographic observations. Besides, their structures concern indistinctly the two different units: the UP and the Ushuaia Peninsula Andesites.

Essentially, the structures related to sinistral strike-slip motion do cut the pluton, but dissected it after its solidification (Figs. 2 and 13). Similar observations were done on plutons of the Beagle suite (coeval with the UP) in Cordillera Darwin (Fig. 1) (Cunningham, 1995; Klepeis et al., 2010; Maloney et al., 2011).

7. Conclusions

The detailed field mapping, along with petrography and the new U–Pb zircon ages allow us to consider UP grew incrementally by successive, although discrete, pulses of magma injection at upper crustal levels, between 75 and 70 Ma. Growth involved two main stages, the first one led to a concentrically zoned ultramafic-mafic section, the second one derived in an intermediate section. Contacts between gabbros/diorites of the ultramafic-mafic section and monzodiorites of the

intermediate section are gradational, including mingling and layering, and suggest momentary simultaneous injection of both sections.

The lithological diversity of the UP resulted from both mid-crustal fractionation and in-situ upper-crustal diversification of I-type, hydrous shoshonitic melts. Scarce peraluminous tonalities resulted by in-situ hybridization with local anatectic partial melts. The mineral and chemical composition of UP differs significantly from that of the neighbouring dykes of the Ushuaia peninsula (UPA), precluding any correlation. Our geochronological results indicate the UPA is at least 6 m.y. older than the UP, inverse to previuos K−Ar results (Acevedo et al., 2002; Peroni et al., 2009).

A high thermal environment allowed the plastic deformation of the country rock around the pluton, facilitating space generation for emplacement. Pre-existing structures controlled magma ascent, and along with post-emplacement strike-slip faulting, contributed to the slightly elongated shape of the pluton.

The lack of metamorphism and subsolidus fabrics in the UP, and of porphyroblast rotation in the aureole, demonstrate it emplaced after peak regional metamorphism, folding and development of penetrative foliation in the country rock, related to the closure of the Rocas Verdes basin. However, at the same time, regional metamorphism in the Cordillera Darwin metamorphic core, 50–60 km to the west, was still occurring, although during concomitant thrusting and denudation (Nelson, 1982; Kohn et al., 1995; Maloney et al., 2011). This is consistent with the higher crustal depth that reached the Cordillera Darwin metamorphic core (~12 kbar; Maloney et al., 2011).

The UP and the other plutons of the suite represent the waning stage of the Late Cretaceous magmatic arc, after which (i.e. 70-68 Ma), a magmatic gap is registered until it resumed backwards to the southern archipelago by 60 Ma (Hervé et al., 1984). Late orogenic setting is the typical tectonic regime for shoshonitic magmatism worldwide (Morrison, 1980).

Declarations of interest

None.

Acknowledgements

MGG want to thank Joaquín Proenza (Univ. of Barcelona) for facilitating microprobe analysis, and Pastoriza family for allowing access to some outcrops. Comments by Paolo Nimis (Univ. of Padova) are also thanked. The following people helped in the field: Fer Santiago, Paula Sotelano, Hernán De Angelis (all from CADIC), Lucas Oliva (UNC), Sabrina Crosta, Gabriel Martin (both from UNTDF), Ale Castro, Berna Urtubey, Ester Verdún, Luisi Luraschi, and the students Caro Malisia (UNSJ), Gastón Porfirio, Coni Lobo, Fede Zuck, Pau Bottone, Marcos Rodríguez from UNTDF. Álvar Sobral and Miguel Barbagallo (CADIC), and José L. Molina (INREMI, Univ. of La Plata) contributed with thin and polished section preparation. Coni Lobo provided some pictures (Fig. 7f), and Ramiro López (CADIC) and Gaby Mosconi helped with figure preparation. Reviewers Julien Leuthold (Institute of Geochemistry and Petrology, ETH Zurich) and Mauricio Calderón (Univ. Andrés Bello) thoroughly contributed to enhance this paper. Handling of this manuscript by Regional Editor Víctor Ramos is also appreciated. MGG greatly appreciates the selfless collaboration of Márcio M. Pimentel with his research since his PhD. This work was partially financed by CONICET (project PIP 6535, M. Escayola).

Appendix A. Supplementary data

Supplementary data to this article can be found online at https://doi.org/10.1016/j.jsames.2018.10.001.

Appendix

Whole rock analyses were carried out at ACME Analytical Labs. Ltd., Canada. Major elements by ICP-ES, trace elements by ICP-MS (pack 4A-4B). Samples were crushed and 250 g splits were pulverized to 85% passing 200 mesh. In both cases 0.2 g sample were analyzed by $LiBO_2$ fusion and dilute nitric digestion. Loss on ignition (LOI) is by weight difference after ignition at 1000 °C. Additional information at www.acmelab.com.

Mineral compositions of UP and Moat pluton samples have been obtained by electron microprobe using a WDS CAMECA SX 50 instrument at the Serveis Cientificotècnics of the Universitat de Barcelona (Spain). Excitation voltage was 20 kV, beam current 15 nA and beam diameter of 3 µm, except for Na. The analytical conditions for Na were excitation voltage 15 kV and beam current 10 nA, beam diameter of 20 µm. All the elements have been measured with counting time of 10 s, with detection limit of 0.1 wt % for all the elements. All the results were corrected for inter-elemental effects by a ZAF-procedure. The standards used were orthoclase (K, Si), wollastonite (Ca), albite (Na, Al), pyrophanite (Mn, Ti), hematite (Fe) and synthetic MgO, Cr_2O_3 and NiO.

U−Pb zircon ages were obtained at Department of Earth and Ocean Sciences, University of British Columbia (Canada), and Geochronology Laboratory of the University of Brasilia (Brazil), by LA-ICP-MS (more details are given in a supplementary file).

References

Acevedo, R.D., 1996. Los mecanismos sustitutivos y los factores de evolución en los anfíboles de la Hornblendita Ushuaia, Tierra del Fuego. Rev. Asoc. Geol. Argent. 51 (1), 69–77.

Acevedo, R.D., Linares, E., Ostera, H.A., Valín-Alberdi, M.L., 2002. La Hornblendita Ushuaia (Tierra del Fuego): geoquímica y Geocronología. Revista Asociación Geológica Argentina 57 (2), 133–142.

Allmendinger, R.W., Cardozo, N.C., Fisher, D., 2013. Structural Geology Algorithms: Vectors & Tensors. Cambridge University Press, Cambridge, England, pp. 289.

Álvarez-Marrón, J., McClay, K.R., Harambour, S., Rojas, L., Skarmeta, J., 1993. Geometry and evolution of the frontal part of the Magallanes foreland thrust and fold belt (Vicuña area) Tierra del Fuego, Southern Chile. AAPG (Am. Assoc. Pet. Geol.) Bull. 77, 1904–1921.

Anderson, J.L., Smith, D.R., 1995. The effect of temperature and fO_2 in the Al-in-hornblende barometer. Am. Mineral. 80, 549–559.

Andújar, J., Scaillet, B., Pichavant, M., Druitt, T., 2015. Differentiation conditions of a basaltic magma from Santorini, and its bearing on the production of andesite in arc settings. J. Petrol. 56, 765–794.

Annen, C., 2011. Implications of incremental emplacement of magma bodies for magma differentiation, thermal aureole dimensions and plutonism–volcanism relationships. Tectonophysics 500, 3–10.

Bachmann, O., Bergantz, G.W., 2004. On the origin of crystal-poor rhyolites: extracted from batholithic crystal mushes. J. Petrol. 45, 1565–1582.

Barbeau, D.L., Gombosi, D.J., Zahid, K.M., Bizimis, M., Swanson-Hysell, N., Valencia, V., Gehrels, G.E., 2009. U-Pb zircon constraints on the age and provenance of the Rocas Verdes basin-fill, Tierra del Fuego, Argentina. G-cubed 10, Q12001. https://doi.org/10.1029/2009GC002749.

Barbey, P., 2009. Layering and schlieren in granitoids: a record of interactions between magma emplacement, crystallization and deformation in growing plutons. Geol. Belg. 12, 109–133.

Barnes, S.J., Roeder, P.L., 2001. The range of spinel compositions in terrestrial mafic and ultramafic rocks. J. Petrol. 42 (12), 2279–2302.

Bartley, J., Coleman, D., Glazner, A., 2008. Incremental pluton emplacement by magmatic crack-seal. Trans. R. Soc. Edinb. Earth Sci. 97, 383–396.

Batanova, V., Pertsev, A., Kamenetsky, V., Ariskin, A., Mochalov, A., Sobolev, A., 2005. Crustal evolution of island-arc ultramafic magma: galmoenan pyroxenite–dunite plutonic complex, koryak highland (far east Russia). J. Petrol. 7, 1345–1366.

Blundy, J., Annen, C., 2016. Crustal magmatic systems from the perspective of heat transfer. Elements 12, 115–120.

Brown, M., Solar, G., 1998. Granite ascent and emplacement during contractional deformation in convergent orogens. J. Struct. Geol. 20, 1365–1393.

Bucholz, C., Eddy, M., Jagoutz, O., Bowring, A., Schmidt, M., Sambuu, O., 2017. Constraining the timescales of magmatic differentiation with U-Pb zircon geochronology. Geology 45 (1), 11–14.

Calderón, M., Fildani, A., Hervé, F., Fanning, C., Weislogel, A., Cordani, U., 2007. Late Jurassic bimodal magmatism in the northern sea-floor remnant of the Rocas Verdes basin, southern Patagonian Andes. J. Geol. Soc. 164, 1011–1022.

Calderón, M., Fosdick, J., Warren, C., Massonne, H.-J., Fanning, C., Fadel Cury, L., Schwanethal, J., Fonseca, P., Galaz, G., Gaytán, D., Hervé, F., 2012. The low-grade Canal de las Montañas Shear Zone and its role in the tectonic emplacement of the Sarmiento Ophiolitic Complex and Late Cretaceous Patagonian Andes orogeny, Chile.

Tectonophysics 524–525, 165–185.
Calderón, M., Hervé, F., Fuentes, F., Fosdick, J., Sepúlveda, F., Galaz, G., 2016. Tectonic evolution of paleozoic and mesozoic metamorphic complexes and the Rocas Verdes ophiolites in southern patagonia. In: In: Ghiglione, M. (Ed.), Geodynamic Evolution of the Southernmost Andes: Connections with the Scotia Arc Springer International Publishing 7-36. ISBN: 978-3-319-39725-2.
Caminos, R., 1980. Cordillera Fueguina. En Geología Regional Argentina. vol. 2. Academia Nacional de Ciencias, Córdoba, pp. 1463–1501.
Cao, S., Torres Carbonell, P., Dimieri, L., 2018. Structural and petrographic constraints on the stratigraphy of the Lapataia formation, with implications for the tectonic evolution of the Fuegian Andes. J. S. Am. Earth Sci. 84, 223–241.
Cardozo, N., Allmendinger, R.W., 2013. Spherical projections with OSXStereonet. Comput. Geosci. 51, 193–205.
Chappell, B., White, A., 1974. Two contrasting granite types. Pac. Geol. 8, 173–174.
Coleman, D.S., Gray, W., Glazner, A.F., 2004. Rethinking the emplacement and evolution of zoned plutons: geochronologic evidence for incremental assembly of the Toulumne Intrusive Suite, California. Geology 32 (5), 433–436.
Cunningham, W.D., 1993. Strike–slip faults in the southernmost Andes and the development of the Patagonian orocline. Tectonics 12, 169–186.
Cunningham, W.D., 1995. Orogenesis at the southern tip of the Americas: the structural evolution of the Cordillera Darwin Metamorphic complex, southernmost Chile. Tectonophysics 244, 197–229.
Curtis, M., Dlowerdew, M., Riley, T., Whitehouse, M., Daly, S., 2010. Andean sinistral transpression and kinematic partitioning in South Georgia. J. Struct. Geol. 32, 464–477.
de Saint Blanquat, M., Horsman, E., Habert, G., Morgan, S., Vanderhaeghe, O., Law, R., Tikoff, B., 2011. Multiscale magmatic cyclicity, duration of pluton construction, and the paradoxical relationship between tectonism and plutonism in continental arcs. Tectonophysics 500, 20–33.
Debon, F., Le Fort, P., 1988. A cationic classification of common plutonic rocks and their magmatic associations: principles, method, applications. Bull. Mineral. 111, 493–510.
Dessimoz, M., Müntener, O., Ulmer, P., 2012. A case for hornblende dominated fractionation of arc magmas: the Chelan Complex (Washington Cascades). Contrib. Mineral. Petrol 163, 567–589.
Drescher-Kaden, F., 1948. Die feldspat-quartz-reactionsgefüge der granite und gneise und ihre genetische bedeutung. Springer, Heidelberg, pp. 259.
Elsztein, C., 2004. Geología y evolución del Complejo Intrusivo de la Península Ushuaia, Tierra del Fuego. Undergraduate Thesis. Facultad de Ciencias Exactas y Naturales, Universidad de Buenos Aires, pp. 103 Unpublished).
Ernst, W., Liu, J., 1998. Experimental phase-equilibrium study of Al- and Ti-contents of calcic amphibole in MORB- A semiquantitative thermobarometer. Am. Mineral. 83, 952–969.
Fiedrich, A., Bachmann, O., Ulmer, P., Deering, C., Kunze, K., Leuthold, J., 2017. Mineralogical, geochemical, and textural indicators of crystal accumulation in the Adamello Batholith (Northern Italy). Am. Mineral. 102, 2467–2483.
Fildani, A., Cope, T., Graham, S., Wooden, J., 2003. Initiation of the Magallanes foreland basin: timing of the southernmost Patagonian Andes orogeny revised by detrital zircon provenance analysis. Geology 31, 1081–1084.
Ghiglione, M., Ramos, V., 2005. Progression of deformation and sedimentation in the southernmost Andes. Tectonophysics 405, 25–46.
Ghiglione, M., Quinteros, J., Yagupsky, D., Bonillo-Martínez, P., Hlebszevtich, J., Ramos, V., Vergani, G., Figueroa, D., Quesada, S., Zapata, T., 2010. Structure and tectonic history of the foreland basins of southernmost South America. J. S. Am. Earth Sci. 29, 262–277.
Glazner, A.F., Bartley, J.M., Coleman, D.S., Gray, W., Taylor, R.Z., 2004. Are plutons assembled over millions of years by amalgamation from small magma chambers? GSA Today (Geol. Soc. Am.) 14 (4/5), 4–11.
Gombosi, D.J., Barbeau Jr., D.L., Garver, J.I., 2009. New thermochronometric constraints on the rapid Paleogene exhumation of the Cordillera Darwin complex and related thrust sheets in the Fuegian Andes. Terra. Nova 21 (6), 507–515.
González Guillot, M., 2009. Estudio petrogenético de plutones de la Cordillera Fueguina entre el lago Fagnano y el canal Beagle y algunas consideraciones sobre las mineralizaciones asociadas. Ph.D. Thesis, Facultad de Ciencias Naturales y Museo, Universidad Nacional de La Plata, pp. 327 Unpublished).
González Guillot, M., 2016. Magmatic evolution of the southernmost Andes and its relation with subduction processes. In: Ghiglione, M. (Ed.), Geodynamic Evolution of the Southernmost Andes: Connections with the Scotia Arc. vols. 37–74 Springer International Publishing ISBN: 978-3-319-39725-2.
González Guillot, M., Acevedo, D., 2009. Facies con biotita y granate en plutones de los Andes Fueguinos de Argentina. 12nd Chilean Geological Congress. Santiago de Chile. S8-014. Actas in CD, pp. 4.
González Guillot, M., Schalamuk, I., 2009. Mineralizaciones metalíferas en rocas ultramáficas de Tierra del Fuego, Argentina. 9th Argentinian Congress of Economic Geology, Actas, pp. 19–24 Catamarca.
González Guillot, M., Escayola, M., Acevedo, R.D., Pimentel, M., Seraphim, G., Proenza, J., Schalamuk, I., 2009. The plutón diorítico Moat: mildly alkaline monzonitic magmatism in the fuegian Andes of Argentina. J. S. Am. Earth Sci. 28, 345–359.
González Guillot, M., Escayola, M., Acevedo, R., 2011. Calc-alkaline rear-arc magmatism in the Fuegian Andes: implications for the mid-Cretaceous tectonomagmatic evolution of southernmost South America. J. S. Am. Earth Sci. 31, 1–16.
González Guillot, M., Prezzi, C., Acevedo, R., Escayola, M., 2012. A comparative study of two rear-arc plutons and implications for the Fuegian Andes tectonic evolution: mount Kranck Pluton and Jeu-Jepén Monzonite, Argentina. J. S. Am. Earth Sci. 38, 71–88.
Grove, T., Elkins-Tanton, L., Parman, S., Chatterjee, N., Müntener, O., Gaetani, G., 2003. Fractional crystallization and mantle melting controls on calc-alkaline differentiation trends. Contrib. Mineral. Petrol. 145, 515–533.
Hervé, F., Nelson, E., Kawashita, K., Suárez, M., 1981. New isotopic ages and the timing of orogenic events in the Cordillera Darwin, southernmost Chilean Andes. Earth Planet Sci. Lett. 55 (2), 257–265.
Hervé, F., Pankhurst, R., Fanning, C., Calderón, M., Yaxley, G., 2007a. The South Patagonian batholith: 150 my of granite magmatism on a plate margin. Lithos 97, 373–394.
Hervé, F., Massonne, H.-J., Calderón, M., Theye, T., 2007b. Metamorphic P-T conditions of late jurassic rhyolites in the Magallanes fold and thrust belt, patagonian Andes, Chile. J. Iber. Geol. 33, 5–16.
Hervé, F., Fanning, C., Pankhurst, R., Mpodozis, C., Klepeis, K., Calderón, M., Thomson, S., 2010. Detrital zircon SHRIMP U-Pb age study of the Cordillera Darwin Metamorphic Complex: sedimentary sources and implications for the evolution of the Pacific margin of Gondwana. J. Geol. Soc. 8, 555–568 London.
Hervé, M., Suárez, M., Puig, A., 1984. The Patagonian Batholith south of Tierra del Fuego, Chile. Timing and tectonic implications. Geol. Soc. London Bull. 141 (5), 909–917.
Hibbard, M.J., 1995. Petrography to Petrogenesis. Prentice Hall, New Jersey, pp. 587.
Holland, T., Blundy, J., 1994. Non-ideal interactions in calcic amphiboles and their bearing on amphibole-plagioclase thermometry. Contrib. Mineral. Petrol. 116, 433–447.
Irvine, T., Baragar, W., 1971. A guide to the chemical classification of the common volcanic rocks. Can. J. Earth Sci. 8, 523–548.
Jagoutz, O., Müntener, O., Ulmer, P., Pettke, T., Burg, J.-P., Dawood, H., Hussain, S., 2007. Petrology and mineral chemistry of lower crustal intrusions: the Chilas Complex, Kohistan (NW Pakistan). J. Petrol. 48, 1895–1953.
John, B., Blundy, J., 1993. Emplacement-related deformation of granitoid magmas, southern Adamello Massif, Italy. GSA Bull. 105, 1517–1541.
John, B., Stünitz, H., 1997. Magmatic fracturing and small-scale melt segregation during pluton emplacement: evidence from the Adamello massif (Italy). In: Bouchez, J. (Ed.), Granite: from Segregation of Melt to Emplacement Fabrics. Kluwer Academic Publications, Dordrecht, pp. 55–74.
Klaver, M., Matveev, S., Berndt, J., Lissenberg, C.J., Vroon, P., 2017. A mineral and cumulate perspective to magma differentiation at Nisyros volcano, Aegean arc. Contrib. Mineral. Petrol. 172 (11–12), 95.
Klepeis, K., 1994. Relationship between uplift of the metamorphic core of the southernmost Andes and shortening in the Magallanes foreland fold and thrust belt, Tierra del Fuego, Chile. Tectonics 13, 882–904.
Klepeis, K., Betka, P., Clarke, G., Fanning, M., Hervé, F., Rojas, L., Mpodozis, C., Thomson, S., 2010. Continental underthrusting and obduction during the cretaceous closure of the Rocas Verdes rift basin, Cordillera Darwin, patagonian Andes. Tectonics 29. https://doi.org/10.1029/2009TC002610. TC3014.
Kohn, M., Spear, F., Harrison, T., Dalziel, I., 1995. $^{40}Ar/^{39}Ar$ geochronology and P-T-t paths from the Cordillera Darwin metamorphic complex, Tierra del Fuego, Chile. J. Metamorph. Geol. 13, 251–270.
Krawckzynski, M., Grove, T., Behrens, H., 2012. Amphibole stability in primitive arc magmas: effects of temperature, H_2O content, and oxygen fugacity. Contrib. Mineral. Petrol. https://doi.org/10.1007/s00410-012-0740-x.
Lameyre, J., 1987. Granites and evolution of the crust. Rev. Bras. Geociencias 17 (4), 349–359.
Lameyre, J., Bowden, P., 1982. Plutonic rock type series: discrimination of various granitoids series and related rocks. J. Volcanol. Geoth. Res. 14, 169–186.
Larocque, J., Canil, D., 2010. The role of amphibole in the evolution of arc magmas and crust: the case from the Jurassic Bonanza arc section, Vancouver Island, Canada. Contrib. Mineral. Petrol. 159, 475–492.
Leake, B.E., 1965. The relationship between tetrahedral aluminium and the maximum possible octahedral aluminium in natural calciferous and subcalciferous amphiboles. Am. Mineral. 50, 843–851.
Leake, B., Woolley, A., Arps, C., Birch, W., Gilbert, M., Grice, J., Hawthorne, F., Kato, A., Kisch, H., Krivovichev, V., Linthout, K., Laird, J., Mandarino, J., Maresch, W., Nickel, E., Rock, N., Schumacher, J., Smith, D., Stephenson, N., Ungaretti, L., Whittaker, E., Youzhi, G., 1997. Nomenclature of amphiboles: report of the subcommittee on amphiboles of the IMA, commission on new minerals and mineral names. Can. Mineral. 35, 219–246.
Leuthold, J., Müntener, O., Baumgartner, L., Putlitz, B., Ovtcharova, M., Schaltegger, U., 2012. Time resolved construction of a bimodal laccolith (Torres del Paine, Patagonia). Earth Planet Sci. Lett. 325–326, 85–92.
Leuthold, J., Müntener, O., Baumgartner, L., Putlitz, B., 2014. Petrological constraints on the recycling of mafic crystal mushes and intrusion of braided sills in the Torres del Paine Mafic Complex (Patagonia). J. Petrol. 55, 917–949.
Leuthold, J., Blundy, J., Brooker, R., 2015. Experimental petrology constraints on the recycling of mafic cumulate: a focus on Cr-spinel from the Rum Eastern Layered Intrusion, Scotland. Contrib. Mineral. Petrol. 170 (2). https://doi.org/10.1007/s00410-015-1165-0. 12.
Mahood, G., Cornejo, P., 1992. Evidence for ascent of differentiated liquids in a silicic magma chamber found in granitic pluton. Royal Society of Edinburgh Transactions. Earth Sci. 83, 63–69.
Maloney, K., Clarke, G., Klepeis, K., Fanning, C., Wang, W., 2011. Crustal growth during back-arc closure: Cretaceous exhumation history of Cordillera Darwin, southern Patagonia. J. Metamorph. Geol. https://doi.org/10.1111/j.1525-1314.00934.x.
Matzel, J., Bowring, S., Miller, R., 2006. Time scales of pluton construction at differing crustal levels: examples from the Mount Stuart and Tenpeak intrusions, North Cascades, Washington. GSA Bull. 118, 1412–1430.
McAtamney, J., Klepeis, K., Mehrtens, C., Thomson, S., Betka, P., Rojas, L., Snyder, S., 2011. Along-strike variability of back-arc basin collapse and the initiation of sedimentation in the Magallanes foreland basin, southernmost Andes (53-54.5°S).

Tectonics 30, TC5001.
McNulty, B.A., Tobisch, O.T., Cruden, A.R., Gilder, S., 2000. Multistage emplacement of the mount givens pluton, central sierra Nevada batholith, California. GSA Bull. 112 (1), 119–135.
Menichetti, M., Tassone, A., Peroni, J., González Guillot, M., Cerredo, M., 2007. Assetto strutturale, petrografia e geofisica della Bahía Ushuaia – Argentina. Rendicont. Soc. Geol. Ital. 4, 259–262.
Menichetti, M., Lodolo, E., Tassone, A., 2008. Structural geology of the Fuegian Andes and Magallanes fold-and-thrust belt- Tierra del Fuego island. Geol. Acta 6, 19–42.
Michel, J., Baumgartner, L., Putlitz, B., Schaltegger, U., Ovtcharova, M., 2008. Incremental growth of the Patagonian Torres del Paine laccolith over 90 k.y. Geology 36 (6), 459–462.
Miller, C.F., Furbish, D., Walker, B., Claiborne, L., Koteas, G.C., Bleick, H., Miller, J., 2011. Growth of plutons by incremental emplacement of sheets in crystal-rich host: evidence from Miocene intrusions of the Colorado River Region, Nevada, USA. Tectonophysics 500, 65–77.
Morimoto, N., 1989. Nomenclature of pyroxenes. Can. Mineral. 27, 143–156.
Morrison, G.W., 1980. Characteristics and tectonics of the shoshonite rock association. Lithos 13, 97–108.
Mukasa, S.B., Dalziel, I.W.D., 1996. Southernmost Andes and south Georgia island, north Scotia ridge: zircon U–Pb and muscovite $^{40}Ar/^{39}Ar$ age constraints on tectonic evolution of southwestern gondwanaland. J. S. Am. Earth Sci. 9, 349–365.
Müntener, O., Kelemen, P., Grove, T., 2001. The role of H2O during crystallization of primitive arc magmas under uppermost mantle conditions and genesis of igneous pyroxenites: an experimental study. Contrib. Mineral. Petrol. 141, 643–658.
Nandedkar, R., Ulmer, P., Müntener, O., 2014. Fractional crystallization of primitive, hydrous arc magmas: an experimental study at 0.7 GPa. Contrib. Mineral. Petrol. 167 (6), 1–20.
Nelson, E.P., 1982. Post-tectonic uplift of the Cordillera Darwin Orogenic Core Complex: evidence for fission track geochronology and closing temperature-time relationships. J. Geol. Soc. 139, 755–761.
Nelson, E.P., Dalziel, I.W.D., Milnes, A.G., 1980. Structural geology of the Cordillera Darwin – collision-style orogenesis in the southernmost Chilean Andes. Eclogae Geol. Helv. 73 (3), 727–751.
Nimis, P., 1995. A clinopyroxene geobarometer for basaltic systems based on crystal-structure modeling. Contrib. Mineral. Petrol. 121, 115–125.
Nimis, P., 1999. Clinopyroxene geobarometry of magmatic rocks. Part 2. Structural geobarometers for basic to acid, tholeiitic and mildly alkaline magmatic systems. Contrib. Mineral. Petrol. 135, 62–74.
Nimis, P., Taylor, W., 2000. Single clinopyroxene thermobarometery for garnet peridotites. Part I. Calibration and testing of the Cr-in-Cpx barometer and an enstatite-in-Cpx thermometer. Contrib. Mineral. Petrol. 139, 541–554.
Olivero, E., Malumián, N., 2008. Mesozoic-cenozoic stratigraphy of the fuegian Andes, Argentina. Geol. Acta 6, 5–18.
Paterson, S.R., Vernon, R.H., Tobisch, O.T., 1989. A review of criteria for the identification of magmatic and tectonic foliations in granitoids. J. Struct. Geol. 11 (3), 349–363.
Paterson, S.R., Vernon, R.H., Fowler Jr., T.K., 1991. Aureole tectonics. In: Kerrick, D.M. (Ed.), Contact Metamorphism. Reviews in Mineralogy 26. Mineralogical Society of America, pp. 673–722.
Paterson, S.R., Fowler Jr., T., Schmidt, K., Yoshinobu, A., Yuan, E.S., Miller, R., 1998. Interpreting magmatic fabric patterns in plutons. Lithos 44, 53–82.
Pattison, D., 2001. Instability of Al_2SiO_5 "triple-point" assemblages in muscovite + biotite + quartz-bearing metapelites, with implications. Am. Mineral. 86, 1414–1422.
Pattison, D.R.M., Tracy, R.J., 1991. Phase equilibria and thermobarometry of metapelites. In: Kerrick, D.M. (Ed.), Contact Metamorphism. Reviews in Mineralogy 26. Mineralogical Society of America, pp. 105–206.
Peroni, J., Tassone, A., Menichetti, M., Cerredo, M., 2009. Geophysical modeling and structure of Ushuaia pluton, fuegian Andes, Argentina. Tectonophysics 476, 436–449.
Petford, N., Cruden, A.R., McCaffrey, K.J.W., Vigneresse, J.-L., 2000. Granite magma formation, transport and emplacement in the Earth's crust. Nature 408, 669–673.
Pichavant, M., Macdonald, R., 2007. Crystallization of primitive basaltic magmas at crustal pressures and genesis of the calc-alkaline igneous suite: experimental evidence from St Vincent, Lesser Antilles arc. Contrib. Mineral. Petrol. 154, 535–558.
Pitcher, W., 1979. The nature, ascent and emplacement of granitic magmas. J. Geol. Soc. London 136, 627–662.
Poblete, F., Roperch, P., Arriagada, C., Ruffet, G., Ramírez de Arellano, C., Hervé, F., Poujol, M., 2016. Late cretaceous–early Eocene counterclockwise rotation of the fuegian Andes and evolution of the patagonia-antarctic peninsula system. Tectonophysics 668–669, 15–34.
Putirka, K., 2008. Thermometers and barometers for volcanic systems. In: Putirka, K., Tepley, F. (Eds.), Minerals, Inclusions and Volcanic Processes. Reviews in Mineralogy and Geochemistry. vol. 69. pp. 61–120.
Ramos, V., Haller, M., Butrón, F., 1986. Geología y evolución tectónica de las islas Barnevelt, Atlántico Sur. Rev. Asoc. Geol. Argent. 41 (1–2), 137–154.
Rickwood, P.C., 1989. Boundary lines between petrologic diagrams which use oxides of major and minor elements. Lithos 22, 247–263.
Ridolfi, F., Renzulli, A., 2012. Calcic amphiboles in calc-alkaline and alkaline magmas: thermobarometric and chemometric empirical equations valid up to 1,130 °C and 2.2 GPa. Contrib. Mineral. Petrol. 163, 877–895.
Ridolfi, F., Renzulli, A., Puerini, M., 2010a. Stability and chemical equilibrium of amphibole in calc-alkaline magmas: an overview, new thermobarometric formulations and application to subduction-related volcanoes. Contrib. Mineral. Petrol. 160, 45–66.
Ridolfi, F., Renzulli, A., Cerredo, M., Oberti, R., Boiocchi, M., Bellatreccia, F., Della Ventura, G., Menichetti, M., Tassone, A., 2010b. Amphibole megacrysts of the cerro Jeu-Jepén pluton: new constraints on magma source and evolution (Fuegian Andes, Argentina). GeoSur. Bolletino di Geofisica Teorica ed Applicata 51, 80–83.
Rollinson, H.R., 1993. Using Geochemical Data: Evaluation, Presentation, Interpretation. Longman Scientific & Technical, England, pp. 352.
Rong, J., Wang, F., 2016. Metasomatic Textures in Granites. Evidence from Petrographic Observation. Science Press Beijing. Springer, pp. 144.
Schmidt, M., 1992. Amphibole composition in tonalite as a function of pressure; an experimental calibration of the Al-in-hornblende barometer. Contrib. Mineral. Petrol. 110, 304–310.
Servicio geológico Minero Argentino (SEGEMAR), 1998. Levantamiento geofísico aéreo, magnetometría área de Tierra del Fuego. Proyecto PASMA. Hojas 5569-II, 5566-I, 5566-II. Escala 1:250000.
SERNAGEOMIN, 2003. Mapa Geológico de Chile. Servicio Nacional de Geología y Minería, Santiago Publicación Geológica Digital, No. 4 (CD-ROM, versión 1.0).
Stern, C., de Wit, M., 2003. Rocas Verdes ophiolites, southernmost South America: remnants of progressive stages of development on oceanic-type crust in a continental margin back-arc basin. In: Dilek, Y., Robinson, P. (Eds.), Ophiolites in Earth History. vol. 218. Geological Society, London, Special Publications, pp. 1–19.
Stern, C.R., Mohseni, P.P., Fuenzalida, P., 1991. Petrochemistry and tectonic significance of lower cretaceous barros arana formation basalts, southernmost chilean Andes. J. S. Am. Earth Sci. 4 (4), 331–342.
Suárez, M., Hervé, M., Puig, A., 1985. Hoja Isla Hoste e islas adyacentes, XII Región. Carta Geológica de Chile 1:250.000, no. 65. Servicio Nacional de Geología y Minería, pp. 113 Chile).
Suárez, M., Hervé, M., Puig, A., 1986. K–Ar dates on granitoids from Archipelago Cabo de Hornos, southernmost Chile. Geol. Mag. 123, 581–584.
Sun, S.S., McDonough, W.F., 1989. Chemical and isotopic systematics of oceanic basalts: implications for mantle composition and processes. In: Saunders, A.D., Norry, M.J. (Eds.), Magmatism in Ocean Basins. vol. 42. Geological Society of London Special Publication, pp. 313–345.
Torres Carbonell, P., Dimieri, L., 2013. Cenozoic contractional tectonics in the Fuegian Andes, southernmost South America: a model for the transference of orogenic shortening to the foreland. Geol. Acta 11, 359–370.
Torres Carbonell, P., Olivero, E., Dimieri, L., 2008. Control en la magnitud de desplazamiento de rumbo del Sistema Transformante Fagnano, Tierra del Fuego, Argentina. Rev. Geol. Chile 35, 63–77.
Torres Carbonell, P., Cao, S., Dimieri, L., 2017. Spatial and temporal characterization of progressive deformation during orogenic growth: example from the Fuegian Andes, southern Argentina. J. Struct. Geol. 99, 1–19.
Ulmer, P., 2007. Differentiation of mantle-derived calc-alkaline magmas at mid to lower crustal levels: experimental and petrologic constraints. Period. Mineral. 76, 309–325.
Vernon, R.H., 2000. Review of microstructural evidence of magmatic and solid-state flow. Electron. Geosci. 5 (2), 1–23.
Vernon, R., Paterson, S., 2008. How late are K-feldspar megacrysts in granites? Lithos 104, 327–336.
Vigneresse, J.L., Clemens, J.D., 2000. Granitic magma ascent and emplacement: neither diapirism nor neutral buoyancy. In: In: Vendeville, B., Mart, Y., Vigneresse, J.L. (Eds.), Slate, Shale and Igneous Diapirs in and Around Europe, vol. 174. Geological Society of London Spec. Publ., pp. 1–19.
Weinberg, R., 2006. Melt segregation structures in granitic plutons. Geology 34 (4), 305–308.
Yang, X.-M., 2017. Estimation of crystallization pressure of granite intrusions. Lithos 286–287, 324–329.